A natural framework for isogeometric fluid-structure interaction based on BEM-shell coupling

Luca Heltai[1a], Josef Kiendl[1b,*], Antonio DeSimone[a], Alessandro Reali[c,d]

[a]*SISSA-International School for Advanced Studies*
via Bonomea 265, 34136 Trieste - Italy
[b]*Institute for Applied Mechanics, Technische Universität Braunschweig*
Bienroder Weg 87, 38106 Braunschweig Germany
[c]*Department of Civil Engineering and Architecture, University of Pavia*
via Ferrata 3, 27100 Pavia - Italy
[d]*Institute for Advanced Study, Technische Universität München*
Lichtenbergstraße 2a, 85748 Garching - Germany

Abstract

The interaction between thin structures and incompressible Newtonian fluids is ubiquitous both in nature and in industrial applications. In this paper we present an isogeometric formulation of such problems which exploits a boundary integral formulation of Stokes equations to model the surrounding flow, and a non linear Kirchhoff-Love shell theory to model the elastic behaviour of the structure. We propose three different coupling strategies: a monolithic, fully implicit coupling, a staggered, elasticity driven coupling, and a novel semi-implicit coupling, where the effect of the surrounding flow is incorporated in the non-linear terms of the solid solver through its damping characteristics. The novel semi-implicit approach is then used to demonstrate the power and robustness of our method, which fits ideally in the isogeometric paradigm, by exploiting only the boundary representation (B-Rep) of the thin structure middle surface.

Keywords: Isogeometric Analysis, Boundary Element Method, Kirchhoff-Love theory, Fluid-Structure Interaction, Incompressible Flows, Shell-BEM coupling

[1]Co-first authors. These authors contributed equally to the article.
[*]Corresponding author. Tel.: +49 0531 39194360
Email addresses: `luca.heltai@sissa.it` (Luca Heltai[1]), `j.kiendl@tu-braunschweig.de` (Josef Kiendl[1]), `antonio.desimone@sissa.it` (Antonio DeSimone), `alereali@unipv.it` (Alessandro Reali)

1. Introduction

One of the most attractive features of isogeometric analysis (IGA) [50, 27] is the ability to bypass mesh generation and to perform direct design-to-analysis simulations, by employing the same class of functions used for geometry parameterization in CAGD packages during the analysis process.

Most modern CAD tools, however, are based on boundary representation (B-Rep) objects, making the use of volume-based finite element isogeometric analysis tools (FE-IGA) less attractive, since they require the extension of the computational domain inside (or outside) the enclosing (or enclosed) CAGD surface.

For thin structures, isogeometric shell models circumvent this issue since they only need a surface description of the structure. For fluid dynamics, isogeometric boundary element methods (IGA-BEM) also circumvent the issue mentioned above by reformulating the volumetric flow problem in boundary integral form. Such dimensionality reduction makes the coupling between boundary integral formulations and shell theory an ideal combination for a large class of fluid-structure interaction (FSI) problems, where thin structures interact with Newtonian incompressible flows, and it fits ideally in the IGA paradigm, by only requiring surface representations for both fluid and structural analyses.

FSI problems have been tackled with many different techniques, ranging from interface tracking, based on Arbitrary Lagrangian Eulerian (ALE) [6, 9, 28, 29, 33, 51] or space–time methods [40, 49, 75, 78, 79, 80], to interface capturing [71] or immersed boundary (IBM) [17, 41, 43, 44, 86], or immersogeometric methods [48, 53]. Most of the FSI applications in the isogeometric community rely on a FE-IGA approximation of the flow equations.

Some early attempts to model FSI problems using only B-Rep representations were common in biological applications [1, 3, 4] and have been recently extended to a purely B-Rep isogeometric paradigm for the simulation of inflatable structures [64, 82, 83].

IGA-BEM and shell techniques have grown separately to mature and efficient simulation techniques. On the IGA-BEM side, a considerable effort has been put in the treatment of singular integration [42, 34], adaptivity [36, 35], multipatch and trimmed surfaces [85, 84], efficient solvers [74, 61], fracture simulations [66, 67], and acoustic wave problems [65]. Flow solvers using IGA-BEM proved to be very effective in the study of vesicles and membranes [3, 4, 52], ship hydrodynamics [57, 69, 12, 11], and rigid wings and sails [60], among many others.

For shell analysis, it can be said that IGA has initiated a renaissance in rotation-free thin shell models motivated by the high continuity of the NURBS discretization, which permits a direct implementation of such models. The first isogeometric formulation for geometrically nonlinear Kirchhoff–Love shells was introduced in [55]. A similar high continuity approach was presented in the pioneering works [26, 25]. These formulations have then been employed for various applications such as wind turbine modeling [8, 10, 47, 58], cloth draping simulations [59], explicit finite strain analysis of membranes [23], PHT-spline shell analysis [62], and fracture modeling within an extended IGA approach [63]. Recently, this formulation was extended to arbitrary hyperelastic materials in [56]. In the case of multipatch structures, the lack of rotational degrees of freedom requires additional treatment at patch connections in order to ensure the necessary C^1-continuity across patch interfaces. Different methods have been proposed, such as the bending strip method [54], penalty formulations as in [2, 19] or a Nitsche formulation as

in [39]. IGA has created a lot of interest and developments not only for thin shell models but also for Reissner-Mindlin shells [14, 31, 30, 81]. Morevoer, a hierarchic family of shells was presented in [32] which includes Kirchhoff-Love, Reissner-Mindlin, and higher order shells. In [13], a blended shell formulation was presented, which is a combination of rotation-free shells [15] in the patch interior and Reissner-Mindlin shells [14] at the boundary. Furthermore, many developments have been done as well on isogeometric solid shells [18, 20, 21, 45, 46]. Thin shell models, as those presented in [55, 56], are purely surface-based, in a sense that the shell is completely defined by its middle surface and the shell kinematics are completely described by the middle surface metric and curvature properties. This allows for a direct integration of IGA into CAD systems [19, 72], it facilitates the coupling of shell structures and fluids in fluid-structure interaction (FSI) applications due to the lack of rotational degrees of freedom [7, 10, 47], and it is perfectly suited for the coupling with an IGA-BEM fluid solver as we propose in this paper.

The rest of this paper is organized as follows. In section 2 we present a brief overview of isogeometric NURBS spaces. The continuous FSI problem we want to tackle is introduced in section 3, and an analysis of the coupling strategies is presented in section 4. Sections 5 and 6 present respectively the numerical treatment of the BEM and Shell parts, while in sections 7 and 8 we present some numerical examples and draw some conclusions.

2. Overview of isogeometric NURBS spaces

Given a nondecreasing knot vector $\Theta = \{k_0, k_1, ..., k_{n+p}\}$, the n B-splines of degree p are defined by the recurrence relation

$$B^{(i,0)}(s) = \begin{cases} 1, & \text{if } k_i \leq s < k_{i+1} \\ 0, & \text{otherwise,} \end{cases} \tag{1}$$

for $p = 0$, while for $p > 0$ we have

$$B^{(i,p)}(s) = \tau^{(i,p)}(s)B^{(i,p-1)}(s) - \tau^{(i+1,p)}(s)B^{(i+1,p-1)}(s), \tag{2}$$

for $i = 0, ..., n - 1$, where

$$\tau^{(i,p)}(s) := \begin{cases} \dfrac{s - k^i}{k^{i+p} - k^i} & \text{if } k^{i+p} \neq k^i \\ 0, & \text{otherwise.} \end{cases} \tag{3}$$

The above recurrence relation can be evaluated in a numerically stable way by the de Boor algorithm (see, for example, [68]). Between two distinct knots, a B-spline is of continuity class $\mathcal{C}^\infty$, at a single knot it is $\mathcal{C}^{p-1}$, and, if a knot is repeated q times, the continuity is reduced to $\mathcal{C}^{p-q}$. A knot can be repeated at most $q = p + 1$ times resulting in a discontinuity ($\mathcal{C}^{-1}$) at that location.

NURBS basis functions are readily obtained from B-Splines by assigning a positive weight w_i to each basis spline function and defining the corresponding NURBS basis function as

$$N^i(s) := \frac{w^i B^{(i,p)}(s)}{\sum_{j=0}^{n-1} w^j B^{(j,p)}(s)}. \tag{4}$$

3

Notice that also the NURBS basis have the partition of unity property, and B-Splines can be considered a special case of NURBS by taking all weights to be identical. Taking two knot vectors Θ_i, with $i = 0, 1$, one can construct the NURBS basis functions for two-dimensional surfaces embedded in three dimensional space by tensor products. Indicating with $\boldsymbol{s} := [s_0, s_1]$ a point in $\Re^2$ and $\boldsymbol{i} := (i_0, i_1)$ a two dimensional multi-index belonging to the set

$$\mathcal{J} := \{\boldsymbol{j} = (j_0, j_1), \quad 0 \le j_k < n_k, \quad k = 0, 1\}, \tag{5}$$

the bi-variate B-Splines and NURBS basis functions are given by

$$B^{\boldsymbol{i},\boldsymbol{p}}(\boldsymbol{s}) := B^{(i_0,p_0)}(s_0)B^{(i_1,p_1)}(s_1), \qquad N^{\boldsymbol{i}}(\boldsymbol{s}) := \frac{w^{\boldsymbol{i}}B^{(\boldsymbol{i},\boldsymbol{p})}(\boldsymbol{s})}{\sum_{\boldsymbol{j}\in\mathcal{J}} w^{\boldsymbol{j}} B^{(\boldsymbol{j},\boldsymbol{p})}(\boldsymbol{s})}, \tag{6}$$

where $\boldsymbol{i}$, $\boldsymbol{p}$ and $\boldsymbol{j}$ are all multi-indices. The multi-index $\boldsymbol{p} = (p_0, p_1)$ is used to keep track of the degrees of the B-Splines in each direction, while $\boldsymbol{n} = (n_0, n_1)$ is used to keep track of the number of basis functions in each direction. Notice that in Equations (4) and (6) we dropped the superscripts p and $\boldsymbol{p}$ from the definition of the NURBS basis functions $N^{\boldsymbol{i}}$, to ease the notation in the rest of the paper.

As a generalization of the one dimensional case, if we take a collection of $n := n_0 n_1$ control points in $\Re^3$, we can represent a two dimensional manifold in a three dimensional space as the image of the map

$$\Re^3 \supset \boldsymbol{x}(\boldsymbol{s}) := \sum_{\boldsymbol{i}\in\mathcal{J}} \boldsymbol{P}^{\boldsymbol{i}} N^{\boldsymbol{i}}(\boldsymbol{s}) \qquad \boldsymbol{s} \in \Re^2. \tag{7}$$

The set of control points $\boldsymbol{P}^{\boldsymbol{i}}$ with $\boldsymbol{i} \in \mathcal{J}$ is usually referred to as *control net*. The domain of the map $\boldsymbol{x}(\boldsymbol{s})$ is the set

$$B^2 := [k_0^0, k_{n_0+p_0}^0] \times [k_0^1, k_{n_1+p_1}^1] \subset \Re^2, \tag{8}$$

where k_j^i is the j-th knot in the i-th knot vector Θ_i.

In what follows, we will use greek indices α, β to indicate components in the two dimensional manifold (i.e., from zero to one) and latin indices to indicate components in the three dimensional embedding manifold.

The tangential vectors on a point on the surface are given by the covariant base vectors $\boldsymbol{g}_\alpha$:

$$\boldsymbol{g}_\alpha(\boldsymbol{s}) = \frac{\partial \boldsymbol{x}(\boldsymbol{s})}{\partial s^\alpha} = \boldsymbol{x}_{,\alpha}(\boldsymbol{s}) \tag{9}$$

Contravariant base vectors $\boldsymbol{g}^\alpha(\boldsymbol{s})$ are obtained through the relation $\boldsymbol{g}^\alpha \cdot \boldsymbol{g}_\beta = \delta_\beta^\alpha$, where δ_β^α is the Kronecker delta. Furthermore, we introduce the unit normal vector $\boldsymbol{g}_3$:

$$\boldsymbol{g}_3(\boldsymbol{s}) = \frac{\boldsymbol{g}_\alpha(\boldsymbol{s}) \times \boldsymbol{g}_\beta(\boldsymbol{s})}{|\boldsymbol{g}_\alpha(\boldsymbol{s}) \times \boldsymbol{g}_\beta(\boldsymbol{s})|}. \tag{10}$$

With the tangential and normal vectors, we can write the first and second fundamental forms of the surface, respectively:

$$g_{\alpha\beta}(\boldsymbol{s}) = \boldsymbol{g}_{\alpha}(\boldsymbol{s}) \cdot \boldsymbol{g}_{\beta}(\boldsymbol{s}) \tag{11}$$

$$b_{\alpha\beta}(\boldsymbol{s}) = \boldsymbol{g}_{\alpha,\beta}(\boldsymbol{s}) \cdot \boldsymbol{g}_3(\boldsymbol{s}) \tag{12}$$

where $g_{\alpha\beta}$ and $b_{\alpha\beta}$ represent the metric and curvature coefficients of the surface.

Integrals on the two-dimensional manifold $\boldsymbol{x}(B^2)$ can be pulled back to the domain B^2 using the standard transformation rule

$$\int_{\boldsymbol{x}(B^2)} f(\boldsymbol{x}) \, \mathrm{d}A = \int_{B^2} f(\boldsymbol{x}(\boldsymbol{s})) J(\boldsymbol{s}) \, \mathrm{d}\boldsymbol{s}, \tag{13}$$

where we indicated with $J(\boldsymbol{s})$ the square root of the determinant of the first fundamental form:

$$J(\boldsymbol{s}) := \sqrt{\det(g_{\alpha\beta}(\boldsymbol{s}))}. \tag{14}$$

A standard (scalar) isogeometric finite dimensional space on a two-dimensional manifold is readily obtained by considering the span of the functions $\phi^{\boldsymbol{i}} := N^{\boldsymbol{i}} \circ \boldsymbol{x}^{-1}$:

$$V_h := \mathrm{span}\{\phi^{\boldsymbol{i}}(\boldsymbol{y})\}_{\boldsymbol{i} \in \mathcal{J}}, \qquad \boldsymbol{y} \in \boldsymbol{x}(B^2) \subset \Re^3, \tag{15}$$

where $\phi^{\boldsymbol{i}}$ are such that

$$\phi^{\boldsymbol{i}}(\boldsymbol{x}(\boldsymbol{s})) = N^{\boldsymbol{i}}(\boldsymbol{s}), \qquad \forall \boldsymbol{s} \in B^2. \tag{16}$$

The dimension of the space V_h is $n = n_0 n_1$ and it is equal to the number of control points that define the geometry of the problem. If we introduce the multi-index set $\mathcal{J}^3$, as done for scalar functions in equation (5),

$$\mathcal{J}^3 := \{\boldsymbol{j} = (j_0, j_1, j_2), \quad 0 \le j_k < 3 \times n_k, \quad k = 0, 1, 2\}, \tag{17}$$

then a finite dimensional space for vector fields of three components is obtained by considering

$$V_h^3 := \mathrm{span}\{\boldsymbol{\Phi}^{\boldsymbol{I}}(\boldsymbol{y})\}_{\boldsymbol{I} \in \mathcal{J}^3} \qquad \boldsymbol{y} \in \boldsymbol{x}(B^2) \subset \Re^3, \tag{18}$$

where the basis functions $\boldsymbol{\Phi}^{\boldsymbol{I}}$ are such that

$$\boldsymbol{\Phi}^{\boldsymbol{I}}(\boldsymbol{y}) := \boldsymbol{e}_a \phi^{\boldsymbol{j}}(\boldsymbol{y}), \qquad \boldsymbol{I} = (3j_0 + a, 3j_1 + a) = 3\boldsymbol{j} + a. \tag{19}$$

The multi index $\boldsymbol{I}$ is meant to transform the multi-index $\boldsymbol{j} \in \mathcal{J}$ plus the component index a into a unique global identifier for the $\boldsymbol{I}$-th basis function. In what follows, we use upper case bold latin indices $\boldsymbol{I}, \boldsymbol{J}$ to indicate the global numbering of the basis functions defining the space V_h^3, lower case latin indices i, j, k to label spacial coordinates in $[0, d)$ and greek indices α, β to label parameter coordinates in $[0, 1]$. Unless otherwise stated, we use Einstein summation convention. A vector function of three components $\boldsymbol{f}(\boldsymbol{x})$ in the space V_h^3 is identified by its coefficient vector $\boldsymbol{f}$ such that

$$V_h^3 \ni \boldsymbol{f}(\boldsymbol{x}) := \boldsymbol{f}^{\boldsymbol{I}} \boldsymbol{\Phi}^{\boldsymbol{I}}(\boldsymbol{x}), \tag{20}$$

where, with a slight abuse of notation, we denote the vector of coefficients $\boldsymbol{f}$ with the same symbol as the function $\boldsymbol{f}(\boldsymbol{x})$ but without the argument "$(\boldsymbol{x})$".

5

3. Fluid-Structure Interaction

We are interested in studying the interaction between a thin deformable elastic body and an incompressible fluid. We consider a model problem where the inertial terms of the fluid are negligible when compared with both the fluid viscosity and the inertial terms of the solid. We assume that the deformable body occupies at time t the region $\Omega^{\mathrm{s}}(t) = \boldsymbol{x}(\Omega_0^{\mathrm{s}}) \subset \Re^3$ and that the rest of the space is entirely occupied by an incompressible fluid whose time dependent domain is $\Omega^{\mathrm{f}}(t) = \Re^3 \setminus \Omega^{\mathrm{s}}(t)$.

The fluid and solid domains are coupled through non-slip conditions and through balance equations across the boundary of the solid domain $\Gamma^{\mathrm{fsi}}(t) := \partial\Omega^{\mathrm{s}}(t)$. We will describe the fluid equations in Eulerian form, where the primal variables are the velocity field of the fluid $\boldsymbol{v}$ and its pressure p at fixed points in space, while we use a Lagrangian description for the the solid, where each point $\boldsymbol{X}$ represents a fixed material point in Ω_0^{s} mapped by the transformation $\boldsymbol{x} : \Omega_0 \times [0, T] \mapsto \Re^d$ to its current location $\boldsymbol{x}(\boldsymbol{X}, t)$ at time t.

For convenience, we introduce the deformation field $\boldsymbol{u}(\boldsymbol{X}, t)$, such that $\boldsymbol{u}(\boldsymbol{X}, t) = \boldsymbol{x}(\boldsymbol{X}, t) - \boldsymbol{X}$. The transformation map $\boldsymbol{x}(\cdot, t) : \Omega_0^{\mathrm{s}} \mapsto \Omega^{\mathrm{s}}(t)$ is assumed to be invertible and bi-lipschitz for each time t in the interval $[0, T]$, i.e., the determinant J of the deformation gradient $\boldsymbol{F} := \mathrm{Grad}\, \boldsymbol{x}(\boldsymbol{X}, t) := \nabla_{\boldsymbol{X}} \boldsymbol{x}(\boldsymbol{X}, t) = \nabla_{\boldsymbol{X}} \boldsymbol{u} + \boldsymbol{I}$ is strictly positive and $\boldsymbol{F}$ is bounded. We denote the gradient and the divergence with respect to the $\boldsymbol{X}$ variable with Grad and Div.

The equations of motion of the system can be written as:

$$-\nabla \cdot \boldsymbol{\sigma} := -\eta \Delta \boldsymbol{v} + \nabla p = 0 \qquad \text{in } \Omega^{\mathrm{f}}(t) \tag{21a}$$

$$\nabla \cdot \boldsymbol{v} = 0 \qquad \text{in } \Omega^{\mathrm{f}}(t) \tag{21b}$$

$$\rho \frac{\partial^2 \boldsymbol{u}}{\partial t^2} - \mathrm{Div}\big(\boldsymbol{F} \cdot \boldsymbol{S}\big) - \boldsymbol{b} = 0 \qquad \text{in } \Omega_0^{\mathrm{s}} \tag{21c}$$

$$J\boldsymbol{\sigma} \cdot \boldsymbol{F}^{-T} \cdot \boldsymbol{\nu}_0 = \boldsymbol{F} \cdot \boldsymbol{S} \cdot \boldsymbol{\nu}_0 \qquad \text{on } \Gamma_0^{\mathrm{fsi}} \tag{21d}$$

$$\boldsymbol{v}(\boldsymbol{x}(\boldsymbol{X}, t), t) = \frac{\partial \boldsymbol{u}(\boldsymbol{X}, t)}{\partial t} =: \dot{\boldsymbol{u}}(\boldsymbol{X}, t) \qquad \text{on } \Gamma_0^{\mathrm{fsi}} \tag{21e}$$

$$\boldsymbol{u}|_{t=0} = \boldsymbol{u}_0 \qquad \text{in } \Omega_0^{\mathrm{s}} \tag{21f}$$

$$\dot{\boldsymbol{u}}|_{t=0} = \boldsymbol{v}_0 \qquad \text{in } \Omega_0^{\mathrm{s}}. \tag{21g}$$

Where $\eta, \boldsymbol{\sigma}$ are the fluid viscosity and Cauchy stress tensor respectively, while $\rho, \boldsymbol{S}$ are the solid density and second Piola-Kirchhoff stress tensor, respectively, and $\boldsymbol{b}$ is a body load acting on the solid, i.e., gravity. The quantities $\boldsymbol{v}_0, \boldsymbol{u}_0, \boldsymbol{\nu}_0$ are the initial solid velocity, initial solid displacement, and outer normal to the reference configuration.

We remark here that at low Reynolds numbers time dependency in the equations of motion of the fluid can only occur due to boundary conditions and through the time dependent changes in the shape of the domain (i.e., $\Omega^{\mathrm{f}}(t)$). For this reason, in equation (21) there are no initial conditions for the fluid velocity, which is assumed to adjust instantaneously to changes in boundary conditions and in domain shape.

Equations (21a) and (21b) represent the conservation of momentum and mass in Eulerian form for a low Reynolds number flow, while equation (21c) is the conservation of momentum for a solid body, written in Lagrangian form.

We will restrict our attention to problems for which $\Omega^s(t)$ is a thin shell and we will consider the Kirchhoff-Love shell theory, where the director, i.e., a vector normal to the middle surface, is assumed to remain normal to the middle surface in the deformed configuration (i.e., parallel to $\boldsymbol{g}_3$). With this assumption, the configuration of the shell is uniquely determined once we know the configuration of its middle surface $\Gamma(t)$, making this an ideal candidate for a coupled FSI problem which requires only a surface description.

To summarise, here are the list of all assumptions we make in our model:

- the inertial terms of the fluid are negligible when compared with both the fluid viscosity and the inertial terms of the solid;

- the transversal dimension h of the solid is much smaller than all other directions, and can be neglected when considering the geometry of the problem;

- the coupling conditions between the solid and the fluid are applied *at the middle surface* $\Gamma(t)$ of the solid.

With these assumptions, the fluid equations reduce to Stokes equations on the domain $\Re^3 \setminus \Gamma(t)$. For a given prescribed velocity on $\Gamma(t)$, we can compute the force per unit area that the fluid exerts on the middle surface of the solid, by pulling the *jump* of the fluid normal stress on $\Gamma(t)$ back to the solid reference configuration.

We define the operator that performs this pull back $D\!N_{\boldsymbol{u}}$, i.e., a *Dirichlet to Neumann map* such that:

$$\boldsymbol{f}^{\text{fsi}} = J D\!N_{\boldsymbol{u}} \boldsymbol{v}_g. \tag{22}$$

Given a Dirichlet datum $\boldsymbol{v}_g$ on the middle surface $\Gamma(t)$, this returns the pull back of the jump of the normal stress associated with the solution of the fluid problem, i.e.,

$$-\nabla \cdot \boldsymbol{\sigma} := -\eta \Delta \boldsymbol{v} + \nabla p = 0 \qquad \text{in } \Re^3 \setminus \Gamma(t) \tag{23a}$$

$$\nabla \cdot \boldsymbol{v} = 0 \qquad \text{in } \Re^3 \setminus \Gamma(t) \tag{23b}$$

$$\boldsymbol{v} = \boldsymbol{v}_g \qquad \text{on } \Gamma(t) \tag{23c}$$

$$J^{-1} \boldsymbol{f}^{\text{fsi}} = [\![\boldsymbol{\sigma}]\!] \cdot \boldsymbol{g}_3 \qquad \text{on } \Gamma(t), \tag{23d}$$

where the symbol $[\![\boldsymbol{\sigma}]\!]$ represents the difference between $\boldsymbol{\sigma}$ across the middle surface $\Gamma(t)$.

For the structural analysis, we consider a Kirchhoff-Love shell in large deformations and small strains, i.e., a St.-Venant-Kirchhoff material model is applied. In the following, we present the weak form of the problem, based on the principal of virtual work.

We will indicate with $\boldsymbol{x}(\boldsymbol{s}, t)$ the current configuration of the middle surface with respect to the curvilinear coordinates $\boldsymbol{s}$, and with $\boldsymbol{X}(\boldsymbol{s})$ the middle surface in the undeformed configuration. Analogously to equations (9)-(12), we define the tangent vectors $\boldsymbol{G}_\alpha$, the unit normal vector $\boldsymbol{G}_3$, the metric coefficients $G_{\alpha\beta}$ and the curvature coefficients $B_{\alpha\beta}$ for the undeformed configuration $\boldsymbol{X}(\boldsymbol{s})$.

As strain measure we use the the Green-Lagrange strain tensor, where only in-plane strains are considered, $\boldsymbol{E} = E_{\alpha\beta} \, \boldsymbol{G}^\alpha \otimes \boldsymbol{G}^\beta$, with:

$$E_{\alpha\beta} = \varepsilon_{\alpha\beta} + \theta^3 \kappa_{\alpha\beta} \tag{24}$$

$$\varepsilon_{\alpha\beta} = \frac{1}{2}(g_{\alpha\beta} - G_{\alpha\beta}) \tag{25}$$

$$\kappa_{\alpha\beta} = B_{\alpha\beta} - b_{\alpha\beta} \tag{26}$$

where $\varepsilon_{\alpha\beta}$ represents the membrane strain while $\kappa_{\alpha\beta}$ describes the change in curvature or bending (pseudo-)strain. As stress measure, we use the energetically conjugate second Piola-Kirchhoff stress tensor $\boldsymbol{S}$:

$$\boldsymbol{S} = \mathbb{C} : \boldsymbol{E} \tag{27}$$

where $\mathbb{C}$ is the fourth-order material tensor. Stresses are represented by the stress resultants $\boldsymbol{n}$ and $\boldsymbol{m}$, which are the normal forces and bending moments, respectively. They are obtained by integrating the constant and the linear parts separately through the shell thickness h as follows:

$$\boldsymbol{n} = \int_{-h/2}^{h/2} \boldsymbol{S}(s^3 = 0) \mathrm{d}s^3 = h \, \hat{\mathbb{C}} : \boldsymbol{\varepsilon} \tag{28}$$

$$\boldsymbol{m} = \int_{-h/2}^{h/2} (\boldsymbol{S} - \boldsymbol{S}(s^3 = 0)) \, s^3 \mathrm{d}s^3 = \frac{h^3}{12} \, \hat{\mathbb{C}} : \boldsymbol{\kappa}, \tag{29}$$

where $\hat{\mathbb{C}}$ is the plane stress material tensor [16]. With membrane strains (25), change in curvature (26), normal forces (28), and bending moments (29), the internal virtual work of the shell can be written as:

$$\delta W_{int} = - \int_{\Gamma_0} (\rho \ddot{\boldsymbol{u}} \cdot \delta \boldsymbol{u} + \boldsymbol{n} : \delta \boldsymbol{\varepsilon} + \boldsymbol{m} : \delta \boldsymbol{\kappa}) \, \mathrm{d}A, \tag{30}$$

where δ denotes that these variables derive from a virtual displacement $\delta \boldsymbol{u}$ and $\mathrm{d}A$ is the differential area element of the middle surface.

The external virtual work is defined as:

$$\delta W_{ext} = \int_{\Gamma_0} \left(\boldsymbol{f}^{\mathrm{fsi}} + \boldsymbol{b} \right) \cdot \delta \boldsymbol{u} \, \mathrm{d}A, \tag{31}$$

where $\boldsymbol{f}^{\mathrm{fsi}}$ is the term coming from the fluid-structure interaction and $\boldsymbol{b}$ some additional body load (e.g., gravity) acting on the shell.

The system is in equilibrium if the sum of internal and external virtual work vanishes

$$\delta W_{int} + \delta W_{ext} = 0, \tag{32}$$

which must hold for an arbitrary variation of $\delta \boldsymbol{u}$.

The final fluid-structure interaction system is given by

$$\int_{\Gamma_0} \left(\rho \ddot{\boldsymbol{u}} \cdot \delta \boldsymbol{u} - J \left(D N_{\boldsymbol{u}} \dot{\boldsymbol{u}} \right) \delta \boldsymbol{u} \right.$$

$$\left. \boldsymbol{n} : \delta \boldsymbol{\varepsilon} + \boldsymbol{m} : \delta \boldsymbol{\kappa} - \boldsymbol{b} \cdot \delta \boldsymbol{u} \right) \mathrm{d} A = 0, \qquad \forall \delta \boldsymbol{u} \in H^2(\Gamma_0) \tag{33a}$$

$$\boldsymbol{u}|_{t=0} = \boldsymbol{u}_0 \qquad \qquad \text{on } \Gamma_0 \tag{33b}$$

$$\dot{\boldsymbol{u}}|_{t=0} = \boldsymbol{v}_0 \qquad \qquad \text{on } \Gamma_0. \tag{33c}$$

An explicit construction of the Dirichlet to Neumann operator $D N_{\boldsymbol{u}}$ is given in section 5. In the general case, we allow the solid to be either free, hinged or clamped. In the first case, the functional space of virtual displacement for which the variational formulation (33) makes sense is

$$V^{\text{free}} := \{ \delta \boldsymbol{u} \in H^2(\Gamma_0) \}, \tag{34}$$

where we denote with $H^k(\Gamma_0)$ the Sobolev space of three-dimensional vector functions on Γ_0 with square integrable weak derivatives up to order k. For the hinged case, we assume that the solid is fixed on the portion $\partial \Gamma_{0,D}$, but it is free to rotate there, and the appropriate functional space would be

$$V^{\text{hinged}} := \{ \delta \boldsymbol{u} \in H^2(\Gamma_0) \text{ s. t. } \delta \boldsymbol{u} = 0 \text{ on } \partial \Gamma_{0,D} \}. \tag{35}$$

If the body is clamped on $\partial \Gamma_{0,D}$, then the correct functional space is given by

$$V^{\text{clamped}} := \{ \delta \boldsymbol{u} \in H^2(\Gamma_0) \text{ s. t. } \delta \boldsymbol{u} = 0, \delta \varphi_n = 0 \text{ on } \partial \Gamma_{0,D} \}, \tag{36}$$

where φ_n describes the normal rotation on the boundary (rotation around the edge) and it is defined by $\varphi_n = \nabla_S \boldsymbol{X} \cdot \boldsymbol{n}_0$, with ∇_S indicating the surface gradient and $\boldsymbol{n}_0$ as the outward normal vector on the boundary.

4. Algorithmic analysis of the FSI problem

We rewrite system (33) in operator form, to make some considerations on possible solution algorithms for the the final fluid-structure interaction problem. We indicate with the functional space V either one of (34), (35) or (36), with V^* its dual space (the space of all linear operators on V) and with $\langle \cdot, \cdot \rangle$ the duality product between V^* and V, i.e.,

$$\langle a, b \rangle := \int_{\Gamma_0} ab \, \mathrm{d} A, \qquad \forall a \in V^*, \forall b \in V. \tag{37}$$

With this notation, (33) can be rewritten as

$$\mathcal{M} \ddot{\boldsymbol{u}} - \mathcal{C}(\boldsymbol{u}) \dot{\boldsymbol{u}} + \mathcal{P}(\boldsymbol{u}) - \mathcal{F} = 0 \qquad \text{in } V^*. \tag{38}$$

9

The operators in equation (38) are defined through their action on arbitrary virtual displacements $\delta\boldsymbol{u}$:

$$\langle\mathcal{M}\ddot{\boldsymbol{u}},\delta\boldsymbol{u}\rangle \qquad := \int_{\Gamma_0}\rho\ddot{\boldsymbol{u}}\cdot\delta\boldsymbol{u}\,\mathrm{d}A \qquad\qquad \forall\delta\boldsymbol{u}\in V \qquad (39)$$

$$\langle\mathcal{C}(\boldsymbol{u})\dot{\boldsymbol{u}},\delta\boldsymbol{u}\rangle \qquad := \int_{\Gamma_0}J\,(D\!N_{\boldsymbol{u}}\dot{\boldsymbol{u}})\,\delta\boldsymbol{u}\,\mathrm{d}A \qquad\qquad \forall\delta\boldsymbol{u}\in V \qquad (40)$$

$$\langle\mathcal{P}(\boldsymbol{u}),\delta\boldsymbol{u}\rangle \qquad := \int_{\Gamma_0}\boldsymbol{n}:\delta\boldsymbol{\varepsilon}+\boldsymbol{m}:\delta\boldsymbol{\kappa}\,\mathrm{d}A \qquad\qquad \forall\delta\boldsymbol{u}\in V \qquad (41)$$

$$\langle\mathcal{F},\delta\boldsymbol{u}\rangle \qquad := \int_{\Gamma_0}\boldsymbol{b}\cdot\delta\boldsymbol{u}\,\mathrm{d}A \qquad\qquad \forall\delta\boldsymbol{u}\in V. \qquad (42)$$

We observe that the fluid operator $\mathcal{C}(\boldsymbol{u})$ is nonlinear in the displacement field $\boldsymbol{u}$, but it is linear in the *velocity* $\dot{\boldsymbol{u}}$, while the elastic operator $\mathcal{P}(\boldsymbol{u})$ is nonlinear in $\boldsymbol{u}$, and, for our choice of elastic constitutive model, it is rate independent.

The presence of the fluid is felt by the structure solely through the non-linear operator $\mathcal{C}(\boldsymbol{u})\dot{\boldsymbol{u}}$, which acts as a damping term for the dynamics of the elastic structure. Classical visco-elastic shells have a very similar structure, where $\mathcal{C}\dot{\boldsymbol{u}}$ is usually taken to be linear in $\dot{\boldsymbol{u}}$, and independent on $\boldsymbol{u}$.

Given the linearity of the problem in both $\ddot{\boldsymbol{u}}$ and $\dot{\boldsymbol{u}}$, a possible solution strategy is to introduce a time discretization $\mathcal{T}:=\{t_0,t_1,\ldots,t_N=T\}$ and write $\boldsymbol{u}_k:=\boldsymbol{u}(t_k)$. At each time step k, we can approximate $\dot{\boldsymbol{u}}_k$ and $\ddot{\boldsymbol{u}}_k$ as a linear combination of the previous solution steps $\boldsymbol{u}_p$ with $p\leq k$, such that the problem reduces to a nonlinear system in $\boldsymbol{u}_k$:

$$\mathcal{M}\ddot{\boldsymbol{u}}_k-\mathcal{C}(\boldsymbol{u}_k)\dot{\boldsymbol{u}}_k+\mathcal{P}(\boldsymbol{u}_k)-\mathcal{F}_k=:\mathcal{R}(\boldsymbol{u}_k)=0 \qquad\text{in }V^*, \qquad (43)$$

whose solution can be formally computed by a Newton iteration method, i.e., given a guess $\boldsymbol{u}_k^0=\boldsymbol{u}_{k-1}$, we compute $\boldsymbol{u}_k^{m+1}=\boldsymbol{u}_k^m+\Delta\boldsymbol{u}_k^m$ where formally

$$\Delta\boldsymbol{u}_k^m=-(D_{\boldsymbol{u}}\mathcal{R}(\boldsymbol{u}_k^m))^{-1}\mathcal{R}(\boldsymbol{u}_k^m), \qquad (44)$$

where $\mathcal{R}(\boldsymbol{u}_k^m)$ is the residual at step m, and the term $D_{\boldsymbol{u}}\mathcal{R}(\boldsymbol{u}_k^m)$ contains the Fréchet derivative of the residual w.r.t. $\boldsymbol{u}$, evaluated at $\boldsymbol{u}_k^m$, i.e.,

$$D_{\boldsymbol{u}}\mathcal{R}(\boldsymbol{u}_k^m)=c_0\mathcal{M}-c_1\mathcal{C}(\boldsymbol{u}_k^m)+D_{\boldsymbol{u}}\mathcal{C}(\boldsymbol{u}_k^m)\dot{\boldsymbol{u}}_k^m+D_{\boldsymbol{u}}\mathcal{P}(\boldsymbol{u}_k^m), \qquad (45)$$

where c_0 and c_1 are the linear coefficients of the $\boldsymbol{u}_k$ term used to approximate $\ddot{\boldsymbol{u}}_k$ and $\dot{\boldsymbol{u}}_k$. The Fréchet derivative in equation (45) translates to the Jacobian of the residual in a finite dimensional setting. If computed directly using equation (45), such a Jacobian can be quite complex to approximate, and several simplifications can be proposed, leading to a Newton-Rapson iteration method in which the Jacobian of the residual is not exact, but only approximate.

Among these methods, the most commonly used are *segregated* methods, where the solution of the fluid system is done separately with respect to the solution of the solid system. These methods are equivalent to a variation of the following systems of equations

$$\mathcal{M}\ddot{\boldsymbol{u}}_k-\mathcal{C}(\boldsymbol{u}_{k-1})\dot{\boldsymbol{u}}_{k-1}+\mathcal{P}(\boldsymbol{u}_k\ \ )-\mathcal{F}_k=0 \qquad\text{in }V^* \qquad (46)$$

$$\mathcal{M}\ddot{\boldsymbol{u}}_k-\mathcal{C}(\boldsymbol{u}_k\ \ )\dot{\boldsymbol{u}}_k\ \ +\mathcal{P}(\boldsymbol{u}_{k-1})-\mathcal{F}_k=0 \qquad\text{in }V^*, \qquad (47)$$

where, in the first case (equation (46)) the fluid terms (i.e., $\mathcal{C}(\boldsymbol{u}_{k-1})\dot{\boldsymbol{u}}_{k-1}$) are computed at the previous time step, and a full nonlinear solution step is iterated on the solid part (solid-dominated segregated FSI schemes), while in the second case (equation (47)) the opposite happens (fluid-dominated segregated FSI schemes).

Due to the nature of the fluid solver, the second family of segregated solvers is in general difficult to achieve for Boundary Element Methods, since it requires computing the Jacobian of the fluid-structure operator $D_{\boldsymbol{u}}\mathcal{C}(\boldsymbol{u}_k^m)$, whose computational cost is in the order of $O(n^3)$, where n is the number of degrees of freedom of the system.

On the other hand, the structure of the problem suggests naturally a semi-implicit solution scheme, in which the nonlinearity of the fluid structure interaction is removed from the system, by evaluating the fluid-structure operator at the previous time step, but retaining the evaluation of the velocity field at the current time step, i.e., solving

$$\mathcal{M}\ddot{\boldsymbol{u}}_k - \mathcal{C}(\boldsymbol{u}_{k-1})\dot{\boldsymbol{u}}_k + \mathcal{P}(\boldsymbol{u}_k) - \mathcal{F}_k = 0 \qquad \text{in } V^*. \tag{48}$$

This solution strategy can be further refined by replacing the computation of $\mathcal{C}(\boldsymbol{u}_{k-1})$ with the current nonlinear iterate $\mathcal{C}(\boldsymbol{u}_k^m)$, resulting in a Newton-Rapson iteration scheme, in which the fully implicit nonlinear system (43) is resolved by replacing the exact Jacobian in equation (45) by an approximation in which $D_{\boldsymbol{u}}\mathcal{C}(\boldsymbol{u}_k^m)\dot{\boldsymbol{u}}_k$ is neglected, i.e.

$$D_{\boldsymbol{u}}\mathcal{R}(\boldsymbol{u}_k^m) \sim c_0\mathcal{M} - c_1\mathcal{C}(\boldsymbol{u}_k^m) + D_{\boldsymbol{u}}\mathcal{P}(\boldsymbol{u}_k^m). \tag{49}$$

The details of the full discrete scheme are given in section 6, where a generalized α-scheme is coupled with the fully implicit solver for the coupled system, with inexact Jacobian given by the discrete version of (49).

5. Isogeometric boundary integral representation of the hydrodynamic equations

The fluid part of the equations of motion takes the form

$$-\eta\Delta\boldsymbol{v} + \nabla p = -\nabla \cdot \boldsymbol{\sigma} = 0 \qquad \text{in } \Omega^{\mathrm{f}}(t) \tag{50a}$$

$$\nabla \cdot \boldsymbol{v} = 0 \qquad \text{in } \Omega^{\mathrm{f}}(t) \tag{50b}$$

$$\boldsymbol{v} = \boldsymbol{v}_g \qquad \text{on } \Gamma(t) \tag{50c}$$

where $\boldsymbol{v}$ and p are the velocity and hydrodynamic pressure fields in the domain $\Omega^{\mathrm{f}}(t) := \Re^3 \setminus \Gamma(t)$, η is the viscosity of the fluid, $\boldsymbol{v}_g$ is the (given) velocity of the middle surface of the shell and $\boldsymbol{\sigma}$ is the Cauchy stress tensor for an incompressible Newtonian fluid:

$$\boldsymbol{\sigma} := -p\boldsymbol{I} + \eta(\nabla\boldsymbol{v} + (\nabla\boldsymbol{v})^T). \tag{51}$$

Equations (50a) and (50b) describe the conservation of linear momentum and volume in the Stokes fluid, while (50c) is a Dirichlet boundary condition. The pressure p can be regarded as the Lagrange multiplier associated with the conservation of volume (50b), and it is uniquely determined by $\boldsymbol{v}$ up to an additive constant.

Following [70] or [73], we can write a boundary integral representation of the solution $\boldsymbol{v}$ and $\boldsymbol{\sigma}$ of system (50) using the free-space Green's functions $\boldsymbol{\mathcal{S}}$ and $\boldsymbol{\mathcal{T}}$:

$$
\begin{aligned}
\mathcal{S}_{ab}(\boldsymbol{r}) &= \frac{1}{8\pi\eta} \left(\frac{r_a r_b}{|\boldsymbol{r}|^3} + \frac{\delta_{ab}}{|\boldsymbol{r}|} \right) \\
\mathcal{T}_{abc}(\boldsymbol{r}) &= -\frac{3}{4\pi} \frac{r_a r_b r_c}{|\boldsymbol{r}|^5},
\end{aligned}
\tag{52}
$$

where $\boldsymbol{r}$ is a shorthand notation for $(\boldsymbol{x} - \boldsymbol{y})$, and $\boldsymbol{\mathcal{S}b}$ and $\boldsymbol{\mathcal{T}b}$ are the velocity and stress fields in free space associated to a Dirac force with intensity $\boldsymbol{b}$ centered in $\boldsymbol{y}$.

Given an arbitrary control volume S such that $S \cap \Gamma(t) = \emptyset$, it is possible to express the velocity $\boldsymbol{v}$ at arbitrary points $\boldsymbol{x} \in S$, as

$$
v_a(\boldsymbol{x}) + \int_{\partial S} \mathcal{T}_{abc}(\boldsymbol{x} - \boldsymbol{y})\nu_b(\boldsymbol{y})v_c(\boldsymbol{y})\,\mathrm{d}\Gamma_y = \int_{\partial S} \mathcal{S}_{ab}(\boldsymbol{x} - \boldsymbol{y})\sigma_{bc}(\boldsymbol{y})\nu_c(\boldsymbol{y})\,\mathrm{d}\Gamma_y.
\tag{53}
$$

If we select $S = \Re^3 \setminus S_\varepsilon$, defined as

$$
S_\varepsilon := \{\boldsymbol{x}(\boldsymbol{s}) + h\boldsymbol{\nu}(\boldsymbol{s}), \qquad \boldsymbol{s} \in B^2, h \in (-\varepsilon/2, \varepsilon/2)\},
\tag{54}
$$

where $\boldsymbol{\nu}$ here and above is $\boldsymbol{g}_3$, i.e., the normal vector to the middle surface, then taking the limit for $\varepsilon \to 0$, the domain S would coincide with $\Gamma(t)$, and equation (53) would collapse to (using compact notation)

$$
\boldsymbol{v}(\boldsymbol{x}) + \int_{\Gamma(t)} \boldsymbol{\mathcal{T}}(\boldsymbol{x} - \boldsymbol{y})\boldsymbol{\nu}(\boldsymbol{y}) [\![\boldsymbol{v}(\boldsymbol{y})]\!]\,\mathrm{d}\Gamma_y = \int_{\Gamma(t)} \boldsymbol{\mathcal{S}}(\boldsymbol{x} - \boldsymbol{y}) [\![\boldsymbol{\sigma}(\boldsymbol{y})]\!]\,\boldsymbol{\nu}(\boldsymbol{y})\,\mathrm{d}\Gamma_y.
\tag{55}
$$

Such a limit may not be well posed if we considered equation (55) *as is*, since we went from a closed surface with no boundaries to a surface with boundaries, and the boundary element method may present singularities on the curves representing the boundary of the two-dimensional middle surface. However, since we impose a no-slip boundary condition on $\Gamma(t)$, the velocity of the fluid on the middle surface coincides with the velocity of the solid on both sides, making the second term on the left hand side in equation (55) identically zero. This term would be responsible for singularities on the one dimensional boundary of the middle surface, which are not there if one considers only the single layer. If we take the trace of this equation on $\Gamma(t)$, the integral on the right hand side becomes weakly singular but integrable, and we obtain a boundary integral equation on the surface $\Gamma(t)$, which can be used to explicitly compute the force per unit area applied by the fluid on the solid $\boldsymbol{f} := [\![\boldsymbol{\sigma}]\!]\,\boldsymbol{\nu}$, solving the following integral equation of the first kind:

$$
\boldsymbol{v}(\boldsymbol{x}) = \int_{\Gamma(t)} \boldsymbol{\mathcal{S}}(\boldsymbol{x} - \boldsymbol{y})\boldsymbol{f}(\boldsymbol{y})\,\mathrm{d}\Gamma_y \qquad \forall \boldsymbol{x} \text{ on } \Gamma(t).
\tag{56}
$$

Such a boundary integral equation generates a fluid velocity field $\boldsymbol{v}$ which is globally in $H^1(\Re^3)$ for any surface traction in $H^{-1/2}(\Gamma)$. An effective way to numerically solve this boundary integral equation is given by the boundary element method, in which $\boldsymbol{v}$ and $\boldsymbol{f}$ are sought for in a finite dimensional space defined on $\Gamma(t)$, and the Dirichlet to Neumann map becomes an invertible matrix.

12

Here we exploit the isogeometric NURBS spaces defined in Section 2 to define the finite dimensional spaces, as well as the discrete versions of the boundary integral equations (56).

We *collocate* the boundary integral equation at n distinct *collocation points* $\{\boldsymbol{x^i}\}_{\boldsymbol{i}\in\mathcal{J}}$, and we restrict both $\boldsymbol{v}(\boldsymbol{x})$ and $\boldsymbol{f}(\boldsymbol{x})$ to live in the finite dimensional space $V_h^3(\Gamma)$:

$$\boldsymbol{v^J}\boldsymbol{\Phi^J}(\boldsymbol{x^i}) = \int_{\Gamma(t)} \boldsymbol{\mathcal{S}}(\boldsymbol{x^I} - \boldsymbol{y})\boldsymbol{f^J}\boldsymbol{\Phi^J}(\boldsymbol{y})\,\mathrm{d}\Gamma_y \qquad \boldsymbol{i} \in \mathcal{J}, \boldsymbol{J} \in \mathcal{J}^3. \tag{57}$$

For each collocation point $\boldsymbol{x^I}$, Equations (57) are systems of 3 equations in $6n$ unknowns (the $3n$ coefficients of $\boldsymbol{v}$ and the $3n$ coefficients of $\boldsymbol{f}$), which can be compactly rewritten as

$$\boldsymbol{M}_c\boldsymbol{v} = \boldsymbol{D}_c\boldsymbol{f} \tag{58}$$

where the (square) matrices $\boldsymbol{M}_c$ and $\boldsymbol{D}_c$ are given by

$$\boldsymbol{M}_c^{(3\boldsymbol{i}+a)\,(\boldsymbol{J})} := \delta_{ab}\Phi_b^{\boldsymbol{J}}(\boldsymbol{x^i}) \tag{59}$$

$$\boldsymbol{D}_c^{(3\boldsymbol{i}+a)\,(\boldsymbol{J})} := \int_{\Gamma(t)} \mathcal{S}_{ab}(\boldsymbol{x^I} - \boldsymbol{y})\Phi_b^{\boldsymbol{J}}(\boldsymbol{y})\,\mathrm{d}\Gamma_y. \tag{60}$$

A common approach for the choice of the collocation points is given by the Greville abscissæ (see, for example, [38], or [5]), which are defined as

$$\boldsymbol{x^i} := \boldsymbol{x}(\boldsymbol{s^i}), \qquad \boldsymbol{s}^{im} := \frac{\sum_{j=1}^p k_{i_m+j}^m}{p}, \tag{61}$$

where $k_{i_m+j}^m$ are the knots of the knot vector Θ_i. Care should be taken in order to avoid collapsing collocation points, which would result in singular matrices.

A discrete version of the Dirichlet to Neumann operator $D\!N_{\boldsymbol{u}}$ is then given by the *damping matrix* $\boldsymbol{C}(\boldsymbol{u})$:

$$\boldsymbol{C}(\boldsymbol{u}) := \boldsymbol{M}_u\boldsymbol{D}_c^{-1}\boldsymbol{M}_c, \tag{62}$$

where the matrix $\boldsymbol{M}_u$ is a pseudo mass matrix, defined as

$$\boldsymbol{M}_u^{\boldsymbol{IJ}} := \int_{\Gamma(t)} \boldsymbol{\Phi^I} \cdot \boldsymbol{\Phi^J}\,\mathrm{d}\Gamma = \int_{\Gamma^0} \boldsymbol{\Phi^I} \cdot \boldsymbol{\Phi^J} J_u\,\mathrm{d}\Gamma. \tag{63}$$

In general it is not necessary to explicitly assemble the matrix $\boldsymbol{C}(\boldsymbol{u})$, as long as we can *compute its action* on arbitrary vectors. Such action requires the solution of the flow problem around $\Gamma(t)$, obtained through the inversion of the (dense) operator $\boldsymbol{D}_c$, pre and post multiplied by two (sparse) matrix multiplications.

6. Isogeometric Galerkin approach for nonlinear shell dynamics

We solve the structural dynamics problem by isogeometric Galerkin discretizations, and rewrite equation (43) in the discrete form:

$$\boldsymbol{R}(\boldsymbol{u}_k) = \boldsymbol{M}_s\ddot{\boldsymbol{u}}_k - \boldsymbol{C}(\boldsymbol{u}_k)\dot{\boldsymbol{u}}_k + \boldsymbol{P}(\boldsymbol{u}_k) - \boldsymbol{F} = \boldsymbol{0}. \tag{64}$$

In equation (64), $\boldsymbol{u}_k, \dot{\boldsymbol{u}}_k, \ddot{\boldsymbol{u}}_k$ indicate the vectors of nodal displacements, velocities, and accelerations at a time step k, $\boldsymbol{P}$ and $\boldsymbol{F}$ are the vectors of internal and external nodal forces, respectively, $\boldsymbol{R}$ is the residual vector, $\boldsymbol{C}$ is the viscous damping matrix, representing the action of the surrounding fluid and obtained according to equation (62), and $\boldsymbol{M}_s$ is the structural mass matrix, obtained in the reference configuration as:

$$\boldsymbol{M}_s^{IJ} := \rho h \int_{\Gamma_0} \boldsymbol{\Phi}^I \cdot \boldsymbol{\Phi}^J \, \mathrm{d}\Gamma \tag{65}$$

with ρ as the density and h as the shell thickness.

As time integration scheme, we use a generalized α-method [24, 27], where the displacements, velocities, and accelerations are interpolated at time instants between two discrete time steps t_{k-1} and t_k as follows:

$$\boldsymbol{u}_{k-1+\alpha_f} = \alpha_f \boldsymbol{u}_k + (1 - \alpha_f)\boldsymbol{u}_{k-1} \ , \tag{66}$$

$$\dot{\boldsymbol{u}}_{k-1+\alpha_f} = \alpha_f \dot{\boldsymbol{u}}_k + (1 - \alpha_f)\dot{\boldsymbol{u}}_{k-1} \ , \tag{67}$$

$$\ddot{\boldsymbol{u}}_{k-1+\alpha_m} = \alpha_m \ddot{\boldsymbol{u}}_k + (1 - \alpha_m)\ddot{\boldsymbol{u}}_{k-1} \ , \tag{68}$$

where the velocity and displacement at time step t_k are defined by a Newmark update:

$$\boldsymbol{u}_k = \boldsymbol{u}_{k-1} + \Delta t \dot{\boldsymbol{u}}_{k-1} + \frac{1}{2}(\Delta t)^2 \left((1 - 2\beta)\ddot{\boldsymbol{u}}_{k-1} + 2\beta \ddot{\boldsymbol{u}}_k \right) \ , \tag{69}$$

$$\dot{\boldsymbol{u}}_k = \dot{\boldsymbol{u}}_{k-1} + \Delta t \left((1 - \gamma)\ddot{\boldsymbol{u}}_{k-1} + \gamma \ddot{\boldsymbol{u}}_k \right) \ , \tag{70}$$

with β and γ as the Newmark parameters and $\Delta t = t_k - t_{k-1}$ as the time step size. Solving for the displacements $\boldsymbol{u}_k$ first, the Newmark updates of velocities and accelerations are obtained as:

$$\dot{\boldsymbol{u}}_k = \frac{\gamma}{\beta \Delta t}(\boldsymbol{u}_k - \boldsymbol{u}_{k-1}) + \left(1 - \frac{\gamma}{\beta} \right)\dot{\boldsymbol{u}}_{k-1} + \left(1 - \frac{\gamma}{2\beta} \right)\Delta t \ddot{\boldsymbol{u}}_{k-1} \ , \tag{71}$$

$$\ddot{\boldsymbol{u}}_k = \frac{1}{\beta(\Delta t)^2}(\boldsymbol{u}_k - \boldsymbol{u}_{k-1}) - \frac{1}{\beta \Delta t}\dot{\boldsymbol{u}}_{k-1} - \left(\frac{1}{2\beta} - 1 \right)\ddot{\boldsymbol{u}}_{k-1} \ . \tag{72}$$

The α and Newmark parameters are determined by the numerical dissipation parameter $\rho_\infty \in [0, 1]$ as follows:

$$\alpha_m = \frac{2 - \rho_\infty}{1 + \rho_\infty} \ , \quad \alpha_f = \frac{1}{1 + \rho_\infty} \ , \quad \beta = \frac{(1 - \alpha_f + \alpha_m)^2}{4} \ , \quad \gamma = \frac{1}{2} - \alpha_f + \alpha_m \ , \tag{73}$$

where $\rho_\infty = 0.5$ is adopted in this paper.

With the interpolated variables (66)-(68), equation (64) is linearized and solved for the displacements, using the approximated Jacobian according to equation (49), which yields the following system of equations:

$$\left(\alpha_m \frac{1}{\beta(\Delta t)^2}\boldsymbol{M}_s - \alpha_f \frac{\gamma}{\beta \Delta t}\boldsymbol{C}(\boldsymbol{u}_{k-1+\alpha_f}^m) + \alpha_f \boldsymbol{K}(\boldsymbol{u}_{k-1+\alpha_f}^m) \right)\Delta \boldsymbol{u}_k^m =$$

$$-\boldsymbol{M}_s \ddot{\boldsymbol{u}}_{k-1+\alpha_m}^m + \boldsymbol{C}(\boldsymbol{u}_{k-1+\alpha_f}^m)\dot{\boldsymbol{u}}_{k-1+\alpha_f}^m - \boldsymbol{P}(\boldsymbol{u}_{k-1+\alpha_f}^m) + \boldsymbol{F}_\alpha \ , \tag{74}$$

with $\boldsymbol{K}$ being the structural stiffness matrix. Equation (74) represents the fully implicit nonlinear system corresponding to (49). As outlined in Section 4, we further consider a

14

semi-implicit (48) and a segregated (46) approach for the fluid-structure coupling. For the semi-implicit approach, the damping matrix $C(u_{k-1+\alpha_f}^m)$ is approximated by $C(u_{k-1})$

$$\left(\alpha_m \frac{1}{\beta(\Delta t)^2} M_s - \alpha_f \frac{\gamma}{\beta \Delta t} C(u_{k-1}) + \alpha_f K(u_{k-1+\alpha_f}^m)\right)\Delta u_k^m =$$
$$-M_s \ddot{u}_{k-1+\alpha_m}^m + C(u_{k-1})\dot{u}_{k-1+\alpha_f}^m - P(u_{k-1+\alpha_f}^m) + F_\alpha , \quad (75)$$

with the effect that the fluid equations have to be assembled and solved only once per time step. For the segregated approach the whole damping term $C(u)\dot{u}$ is considered constant during one time step. In this case, the contribution from the fluid can be considered as an additional external force $F_\alpha^{fsi} = C(u_{k-1})\dot{u}_{k-1}$, and the damping term on the left hand side of (74) vanishes:

$$\left(\alpha_m \frac{1}{\beta(\Delta t)^2} M_s + \alpha_f K(u_{k-1+\alpha_f}^m)\right)\Delta u_k^m = -M_s \ddot{u}_{k-1+\alpha_m}^m + F_\alpha^{fsi} - P(u_{k-1+\alpha_f}^m) + F_\alpha .$$
$$(76)$$

The internal force vector $P(u)$ and stiffness matrix $K(u)$ are obtained by linearization of the static terms of internal virtual work of the shell model (30) with respect to discrete displacement variables u_I and u_J:

$$P^I = -\int_A \left(n : \frac{\partial \varepsilon}{\partial u_I} + m : \frac{\partial \kappa}{\partial u_I}\right) \mathrm{d}A \qquad (77)$$

$$K^{IJ} = \int_A \left(\frac{\partial n}{\partial u_J} : \frac{\partial \varepsilon}{\partial u_I} + n : \frac{\partial^2 \varepsilon}{\partial u_I \partial u_J} + \frac{\partial m}{\partial u_J} : \frac{\partial \kappa}{\partial u_I} + m : \frac{\partial^2 \kappa}{\partial u_I \partial u_J}\right) \mathrm{d}A \qquad (78)$$

with

$$\frac{\partial n}{\partial u_J} = h\, \hat{\mathbb{C}} : \frac{\partial \varepsilon}{\partial u_J} \qquad (79)$$

$$\frac{\partial m}{\partial u_J} = \frac{h^3}{12}\, \hat{\mathbb{C}} : \frac{\partial \kappa}{\partial u_J} \qquad (80)$$

For the discrete model, C^1-continuity of the basis functions is required since second derivatives appear in the definition of the curvatures (12). NURBS-based isogeometric discretizations provide the necessary continuity and allow a straightforward implementation of this formulation. The control point displacements are identified as the displacement variables u_I. The detailed linearization of the strain variables ε and κ with respect to u_I and u_J is given in Appendix A.

7. Numerical tests

In this section, we apply the presented methods to different numerical tests. First, we consider the free vibration of a beam immersed in a fluid and use it to compare the different coupling strategies. Furthermore, we consider a structure which is deformed by externally applied loads and the damping effect of the surrounding fluid and, finally, we consider a free fall problem.

7.1. Vibration of a cantilever inside a viscous fluid

We consider a cantilever plate surrounded by a viscous fluid. The plate dimensions are $1m \times 0.1m \times 1mm$ (*length $\times$ width $\times$ thickness*). The material parameters are $E = 210.1 \cdot 10^{10} Pa, \nu = 0.3, \rho = 7850 kg/m^3$. The plate is clamped at the left edge and initially deformed corresponding to a static load of $225 N/m$ at the right edge (tip). At time $t = 0$, the load is removed and the vibrations of the plate are observed by plotting the tip displacement. In Figure 1, we plot the tip displacement for different viscosities $\eta = \{10, 1, 10^{-1}, 10^{-3}\} Pa \cdot s$, using a time step of $\Delta t = 0.01s$. The typical patterns of damped vibration can be observed, with an over-damping in the very viscous case ($\eta = 10$), and damped oscillations for the other cases which converge towards the undamped vibration solution for very small viscosities. For comparison, we also perform a purely structural dynamics simulation with no damping, see Figure 2. We measure the natural frequencies (averaged over the first 7 periods) obtained in these simulations and report them in Table 1, which shows that the frequencies of the oscillations in the fluid-structure interaction model are converging to that of the undamped vibration case as the viscosity η converges to zero. We can also observe that, as to be expected, the frequency diminishes as the dissipation increases. Furthermore, we compute the analytical solution of an undamped vibrating cantilever beam, which is given by $f_{ref} = \dfrac{1.875^2}{2\pi L^2}\sqrt{\dfrac{Eh^2}{12\rho}}$, where L is the beam length. It should be noted that the analytical solution is based on linear beam theory, while the numerical solutions are obtained with a nonlinear shell formulation. Since, to the best of our knowledge, there is no analytical solution available for the free vibration of a shell with nonlinear kinematics, we use this beam solution as an approximate reference solution showing that our results are in a physically sound range. The analytical frequency obtained from linear beam theory is $f_{ref} = 2.6418 Hz$, showing good agreement with the numerical results, considering the differences in the underlying models.

η $[Pa \cdot s]$:	1	10^{-1}	10^{-3}	Undamped Vibration
f $[1/s]$:	2.6254	2.7055	2.7254	2.7284

Table 1: Vibration frequencies (averaged over the first 7 periods) for different values of fluid viscosity and for undamped vibration.

All results in Figure 1 have been obtained by the semi-implicit approach (48). In a next step, we use this example in the very viscous case ($\eta = 10\,Pa \cdot s$) in order to compare the three different coupling approaches, i.e., the fully implicit (49), the semi-implicit (48), and the segregated approach (46). For all cases, we consider different time steps $\Delta t = \{0.01, 0.05, 0.1\}s$. The results are gathered in Figure 3. As can be seen, the results for the fully implicit and the semi-implicit approach are identical for all cases. The segregated approach yields stable results only for the smallest time step, while strong spurious oscillations appear when the time step is increased. We highlight that the computational cost of the semi-implicit approach is the same as in the segregated

(a) $\eta = 10\,Pa \cdot s$ (b) $\eta = 1\,Pa \cdot s$

(c) $\eta = 0.1\,Pa \cdot s$ (d) $\eta = 0.001\,Pa \cdot s$
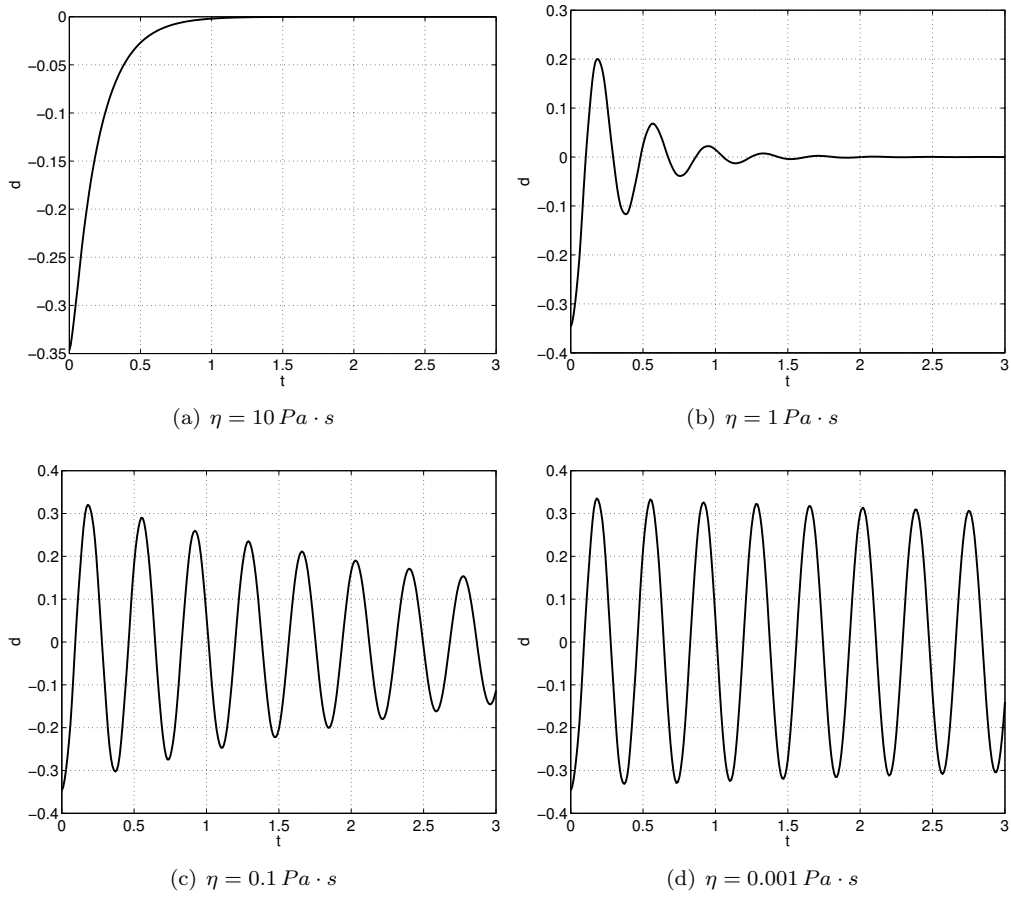
Figure 1: Vibration of a cantilever immersed in a viscous fluid. Tip displacement for different viscosities and $\Delta t = 0.01s$, obtained using the semi-implicit approach.
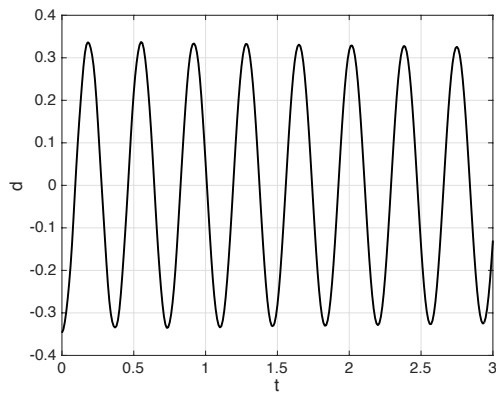
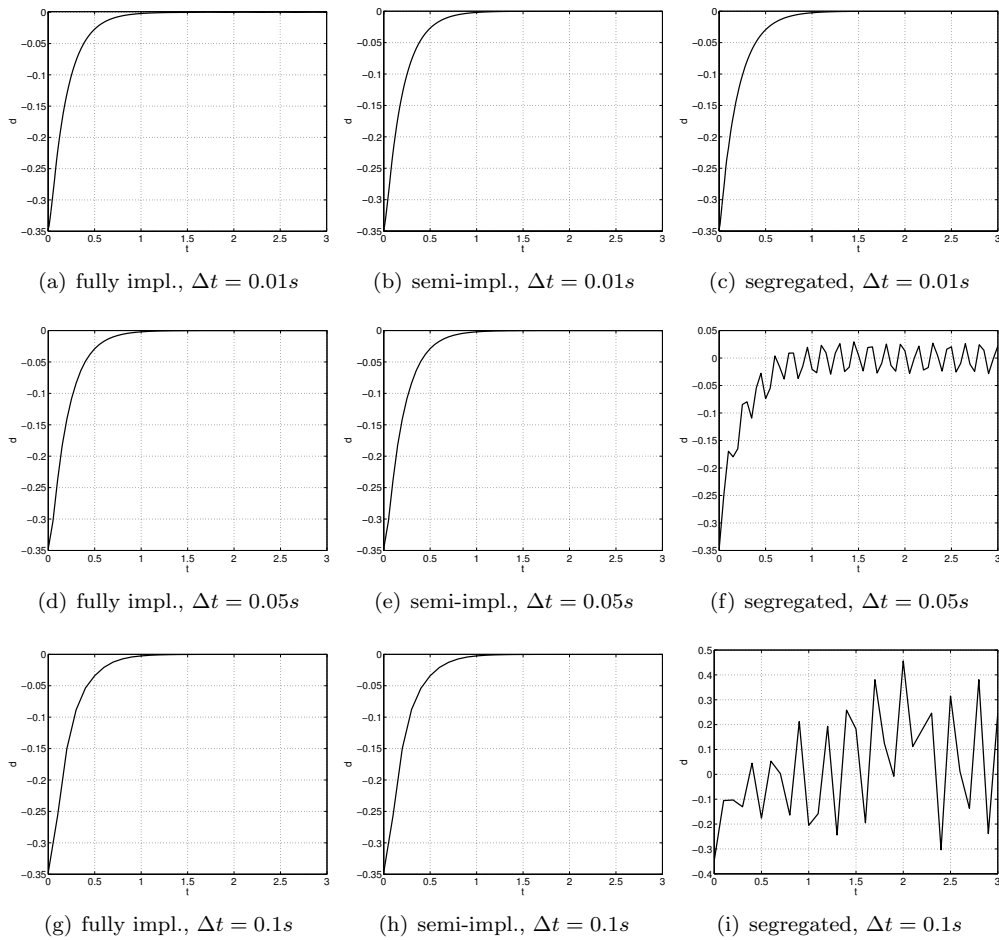Figure 2: Undamped vibration of a cantilever, obtained by a pure structural dynamics computation.

17

Figure 3: Vibration of a cantilever immersed in a viscous fluid. Tip displacement for $\eta = 10$ using different coupling approaches and different time steps: fully implicit (left), semi-implicit (middle), segregated (right), with time steps $\Delta t = \{0.01, 0.05, 0.1\}s$ (top, middle, bottom).
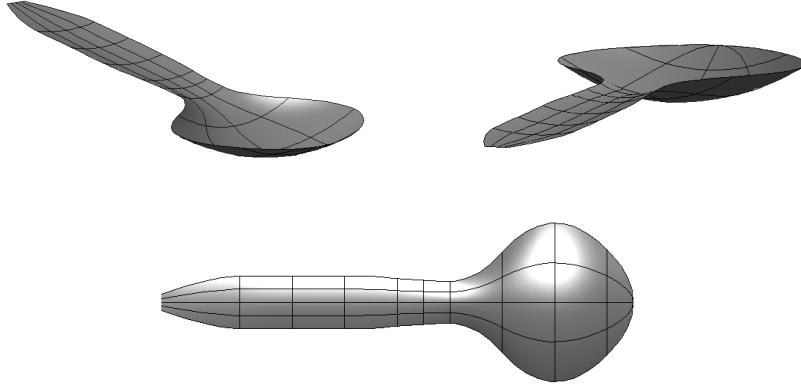
Figure 4: Honey-spoon geometry.

approach, assembling the matrices of the fluid problem only once per time step, and, therefore, significantly less than in the fully implicit approach where the fluid problem matrices are assembled in each Newton iteration. Accordingly, the semi-implicit approach appears to be a very efficient alternative combining the cost-effectiveness of the segregated approach with the accuracy and stability of the fully implicit approach. For the remainder of this paper, we use the semi-implicit formulation in all computations.

7.2. Honey-spoon

In this example, we model the fluid-structure interaction of a spoon moving through honey. The spoon geometry is shown in Figures 4 and 5, it is $4.5\,cm$ long with a thickness $h = 0.2\,mm$ and material parameters $E = 2.8 \cdot 10^9\,N/mm^2, \nu = 0.39, \rho = 1.13\,kg/m^3$. The viscosity of the honey is taken as $\eta = 5.0\,Pa \cdot s$. The problem setup and boundary conditions are shown in Figure 5, with $F = 7000\,N/m^2$, corresponding to a total load of $0.177\,N$. In Figure 6 the deformation at different time steps is displayed, where a time step of $\Delta t = 0.1\,s$ has been used. Figure 7 presents the details of the flow streamlines and velocity magnitude for two significant time steps.

7.3. Falling cap

In this final example, we apply our method to the simulation of falling objects. Such problems are especially challenging in terms of fluid mesh generation and mesh update when using ALE approaches [37, 76, 77]. In [22, 44, 86], such problems were treated by immersed approaches, which avoid the difficulties of mesh update or remeshing but still require the discretization of a large fluid domain, whose size depends on the time interval to be observed. Using the approach presented in this paper, the computational
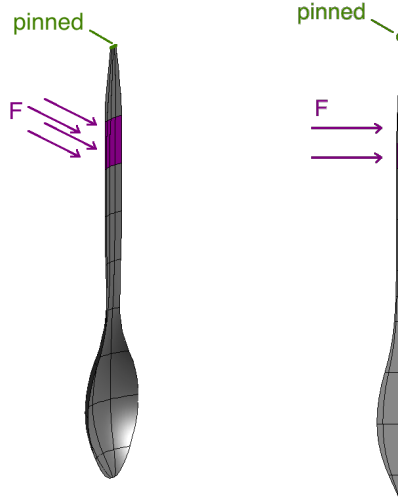
Figure 5: Honey-spoon problem setup.

domain is always confined to the surface model of the structure and is independent on the "falling time". The object under consideration is a cap as shown in Figure 8(a). The structure's material parameters are $E = 2.8 \cdot 10^5 \, N/mm^2, \nu = 0.39, \rho = 1.13 \, kg/m^3$ and the thickness is $h = 1.0 \, mm$. The structure is immersed into water with $\eta = 9.0 \cdot 10^{-3} Pa \cdot s$ and subjected to gravity. A time step of $\Delta t = 1.0 \, s$ is used for the analysis and the results are depicted in Figure 8. We can observe a combination of deformation modes, i.e., a rotation into the upright position and the deformation due to the flexibility of the structure. Figure 9 presents the details of the relative flow streamlines and relative velocity magnitude for two significant time steps.

8. Conclusions

In this paper, we have presented an isogeometric analysis framework to deal with a special class of FSI problems, where the fluid is represented by a Stokes flow and the structure by a shell. The proposed framework can be defined "truly isogeometric" because it is entirely based on bivariate geometries, as those immediately given by CAD B-rep descriptions, given the shell nature of the considered structure and the fact that the fluid equations are solved by isogeometric boundary elements. This allows to completely circumvent the mesh generation process in many situations. In addition, the use of boundary elements may significantly limit the dimension of the discrete problem, in particular when large fluid domains are studied as in the case of falling objects.

For the solution of the coupled problem, we have chosen to adopt a semi-implicit algorithm where the effect of the surrounding flow is incorporated in the non-linear terms of the solid solver through its damping characteristics. This strategy seems capable of favourably combining the accuracy and stability of a fully implicit method with the cost-efficiency of a segregated approach.

(a) $t = 0s$

(b) $t = 0.1s$

(c) $t = 0.2s$

(d) $t = 0.3s$

(e) $t = 0.4s$

(f) $t = 0.5s$

(g) $t = 0.6s$

(h) $t = 0.7s$

(i) $t = 0.8s$

(j) $t = 0.9s$

(k) $t = 1.0s$

(l) $t = 1.1s$
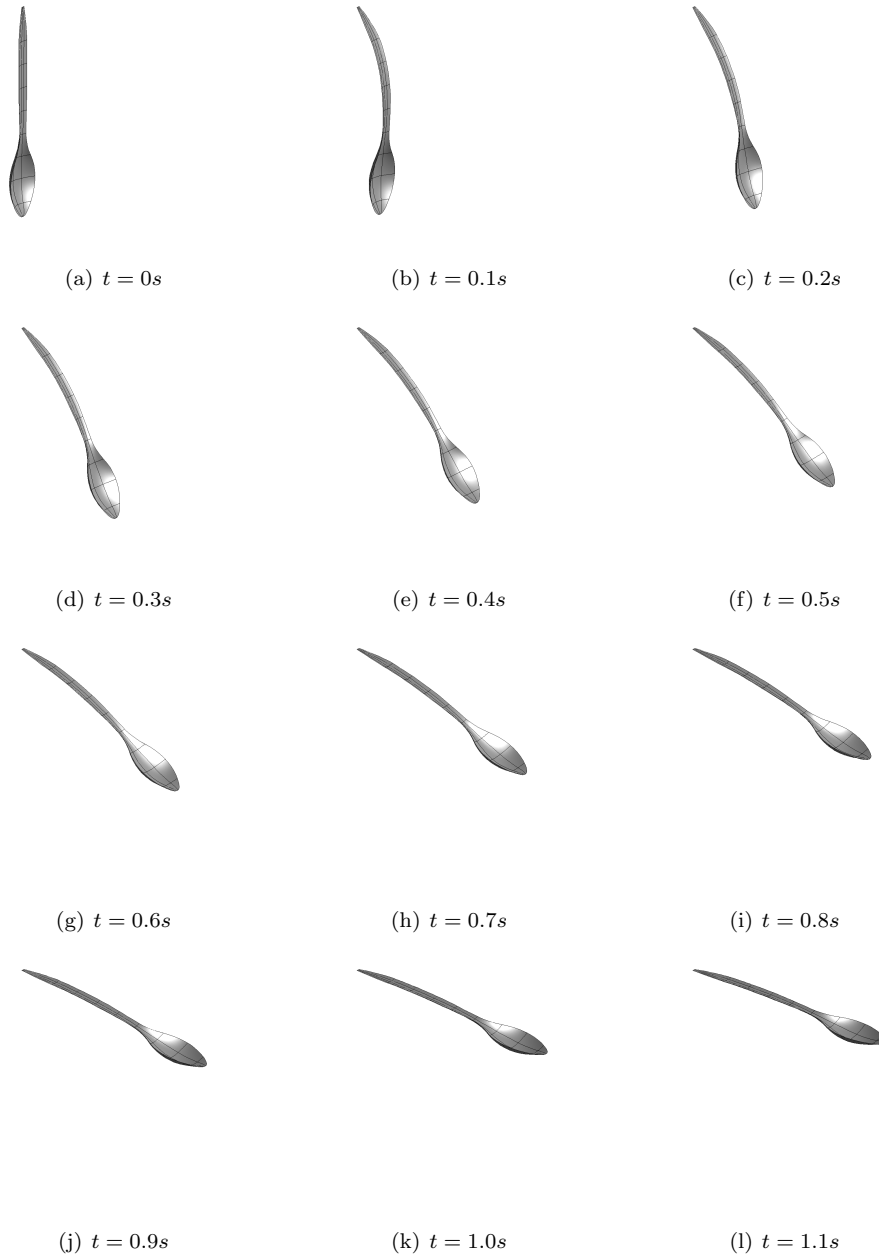
Figure 6: Honey-spoon deformation plots.
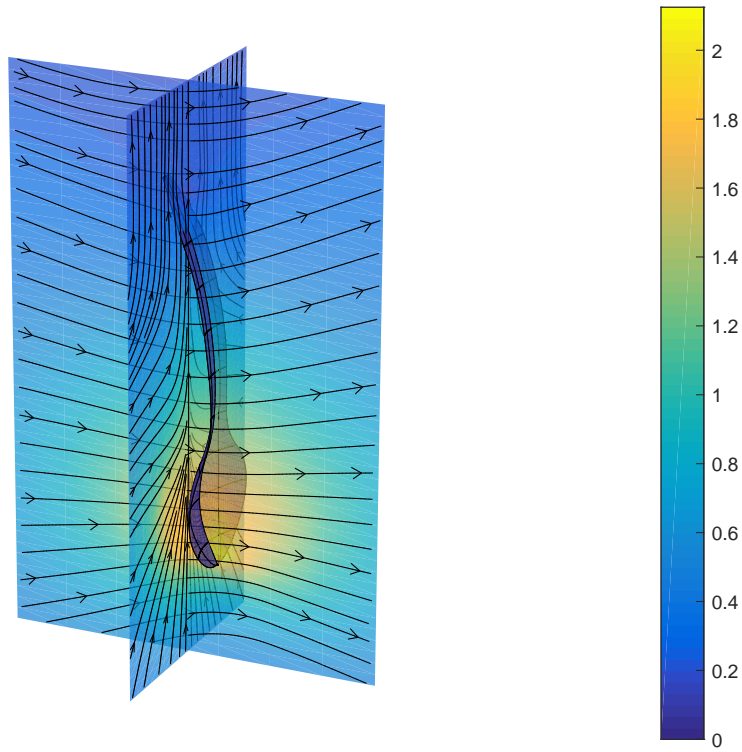
(a) $t = 0.1s$
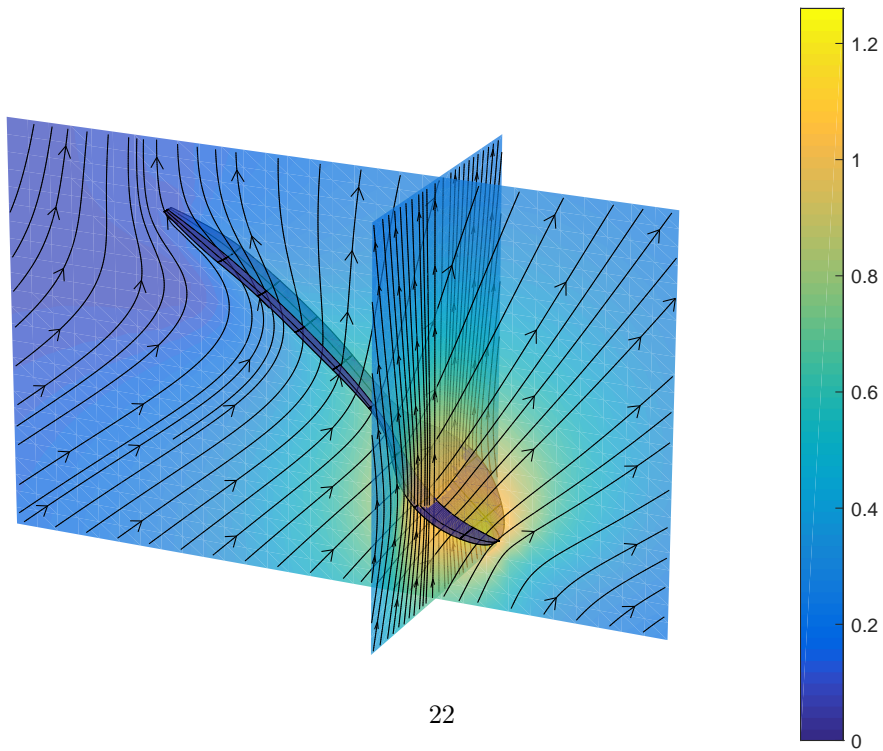
(b) $t = 0.7s$

Figure 7: Honey-spoon streamline plots. Streamlines and velocity magnitude plots, projected on two perpendicular planes. Velocity is measured in m/s.
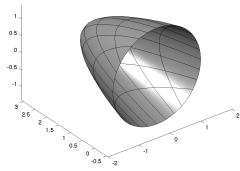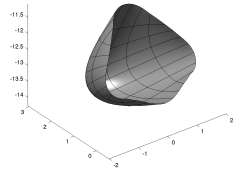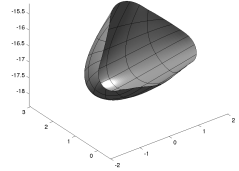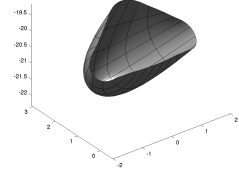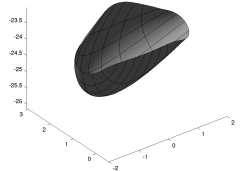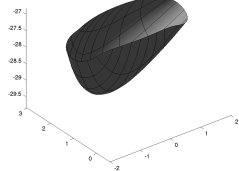
(a) $t = 1s$
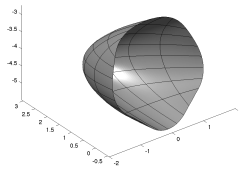
(b) $t = 51s$
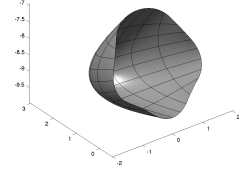
(c) $t = 101s$

(d) $t = 151s$

(e) $t = 201s$

(f) $t = 251s$

(g) $t = 301s$

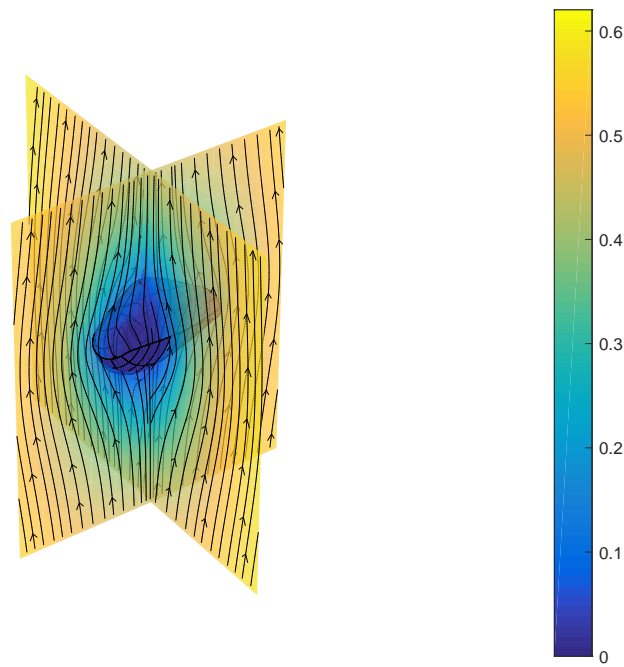(h) $t = 351s$
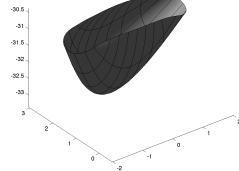
(i) $t = 401s$
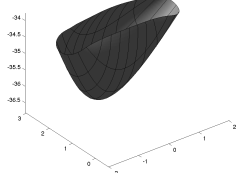
(j) $t = 451s$
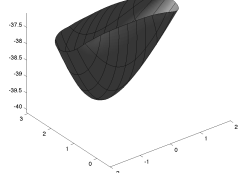
(k) $t = 501s$
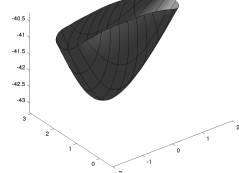
(l) $t = 551s$

Figure 8: Falling cap in water.

23
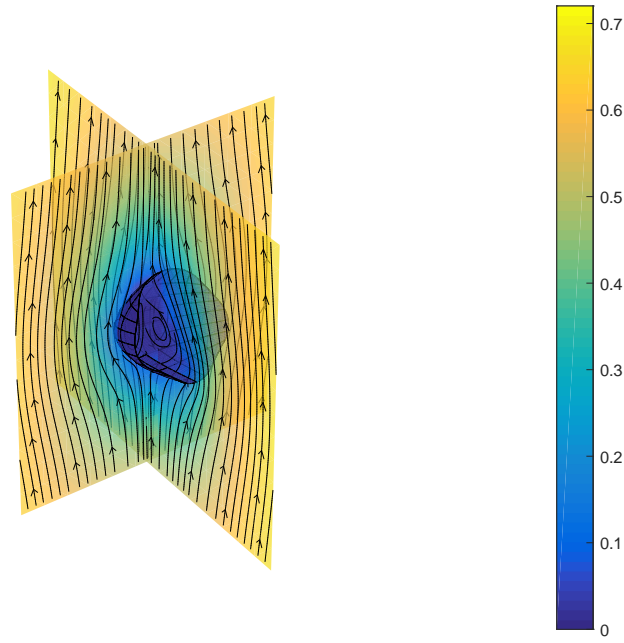
(a) $t = 101s$

(b) $t = 301s$

Figure 9: Falling cap streamline plots. Streamlines and velocity magnitude plots for the relative velocity, projected on two perpendicular planes. Velocity is measured in m/s.

Several numerical tests have been presented, showing the potential of the proposed analysis framework. The extension to more complex situations, like, e.g., cell motion, and the study of the convergence properties of the model will be the subject of forthcoming research.

Acknowledgements

Appendix A. Linearization of strain variables

We begin with the linearization of the displacement vector $\boldsymbol{u}$, which, in discrete form, is defined as:

$$\boldsymbol{u} = \sum_{a}^{n_{cp}} N^a \hat{\boldsymbol{u}}^a \tag{A.1}$$

where n_{cp} is the number of control points, N^a are the NURBS basis functions, and $\hat{\boldsymbol{u}}^a$ are the nodal displacement vectors with components $\hat{u}_i^a$ ($i = 1, 2, 3$) referring to the global $x-, y-, z-$components. The global degree of freedom number $\boldsymbol{I}$ of a nodal displacement is defined by $\boldsymbol{I} = 3(a - 1) + i$, such that $u_{\boldsymbol{I}} = \hat{u}_i^a$. The variation with respect to $u_{\boldsymbol{I}}$ is denoted by $(\cdot),_{\boldsymbol{I}}$ for a compact notation and we obtain:

$$\frac{\partial \boldsymbol{u}}{\partial u_{\boldsymbol{I}}} = \boldsymbol{u},_{\boldsymbol{I}} = N^a \boldsymbol{e}_i \tag{A.2}$$

with $\boldsymbol{e}_i$ representing the global cartesian base vectors. For the second derivatives we obtain:

$$\frac{\partial^2 \boldsymbol{u}}{\partial u_{\boldsymbol{I}} \partial u_{\boldsymbol{J}}} = \boldsymbol{u},_{\boldsymbol{I}\boldsymbol{J}} = \boldsymbol{0} \tag{A.3}$$

Since variations with respect to $u_{\boldsymbol{I}}$ vanish for all quantities of the undeformed configuration, we obtain for the variation of $\boldsymbol{x}$:

$$\boldsymbol{x},_{\boldsymbol{I}} = \boldsymbol{u},_{\boldsymbol{I}} = N^a \boldsymbol{e}_i \tag{A.4}$$

$$\boldsymbol{x},_{\boldsymbol{I}\boldsymbol{J}} = \boldsymbol{u},_{\boldsymbol{I}\boldsymbol{J}} = \boldsymbol{0} \tag{A.5}$$

Accordingly, we get the variations of the base vectors $\boldsymbol{g}_\alpha$ as:

$$\boldsymbol{g}_\alpha,_{\boldsymbol{I}} = N,_\alpha^a \, \boldsymbol{e}_i \tag{A.6}$$

$$\boldsymbol{g}_\alpha,_{\boldsymbol{I}\boldsymbol{J}} = \boldsymbol{0} \tag{A.7}$$

and for $\boldsymbol{g}_{\alpha,\beta}$:

$$\boldsymbol{g}_{\alpha,\beta,\boldsymbol{I}} = N_{,\alpha\beta}^a\,\boldsymbol{e}_i \tag{A.8}$$

$$\boldsymbol{g}_{\alpha,\beta,\boldsymbol{I}\boldsymbol{J}} = \boldsymbol{0} \tag{A.9}$$

With (A.6)-(A.7) and $u_{\boldsymbol{J}} = \hat{u}_j^b$ we can express the variations of the metric coefficients $g_{\alpha\beta} = \boldsymbol{g}_\alpha \cdot \boldsymbol{g}_\beta$:

$$g_{\alpha\beta,\boldsymbol{I}} = N_{,\alpha}^a\,\boldsymbol{e}_i \cdot \boldsymbol{g}_\beta + N_{,\beta}^a\,\boldsymbol{e}_i \cdot \boldsymbol{g}_\alpha \tag{A.10}$$

$$g_{\alpha\beta,\boldsymbol{I}\boldsymbol{J}} = (N_{,\alpha}^a\,N_{,\beta}^b + N_{,\beta}^a\,N_{,\alpha}^b)\delta_{ij} \tag{A.11}$$

The variations of the unit normal vector $\boldsymbol{g}_3$ are more involved and, therefore, we introduce the auxiliary variables $\tilde{\boldsymbol{g}}_3$ and $\bar{g}_3$

$$\tilde{\boldsymbol{g}}_3 = \boldsymbol{g}_1 \times \boldsymbol{g}_2 \tag{A.12}$$

$$\bar{g}_3 = \sqrt{\tilde{\boldsymbol{g}}_3 \cdot \tilde{\boldsymbol{g}}_3} \tag{A.13}$$

such that $\boldsymbol{g}_3$ can be written as:

$$\boldsymbol{g}_3 = \frac{\tilde{\boldsymbol{g}}_3}{\bar{g}_3} \tag{A.14}$$

In the following, we first compute the variations of the auxiliary variables which are then used for further derivations. It is convenient to follow this approach also in the implementation since these intermediate results are needed several times. We first derive the variations of $\tilde{\boldsymbol{g}}_3$:

$$\tilde{\boldsymbol{g}}_{3,\boldsymbol{I}} = \boldsymbol{g}_{1,\boldsymbol{I}} \times \boldsymbol{g}_2 + \boldsymbol{g}_1 \times \boldsymbol{g}_{2,\boldsymbol{I}} \tag{A.15}$$

$$\tilde{\boldsymbol{g}}_{3,\boldsymbol{I}\boldsymbol{J}} = \boldsymbol{g}_{1,\boldsymbol{I}} \times \boldsymbol{g}_{2,\boldsymbol{J}} + \boldsymbol{g}_{1,\boldsymbol{J}} \times \boldsymbol{g}_{2,\boldsymbol{I}} \tag{A.16}$$

which are used for the variations of $\bar{g}_3$:

$$\bar{g}_{3,\boldsymbol{I}} = \boldsymbol{g}_3 \cdot \tilde{\boldsymbol{g}}_{3,\boldsymbol{I}} \tag{A.17}$$

$$\bar{g}_{3,\boldsymbol{I}\boldsymbol{J}} = \bar{g}_3^{-1}(\tilde{\boldsymbol{g}}_{3,\boldsymbol{I}\boldsymbol{J}} \cdot \tilde{\boldsymbol{g}}_3 + \tilde{\boldsymbol{g}}_{3,\boldsymbol{I}} \cdot \tilde{\boldsymbol{g}}_{3,\boldsymbol{J}} - (\tilde{\boldsymbol{g}}_{3,\boldsymbol{I}} \cdot \boldsymbol{g}_3)(\tilde{\boldsymbol{g}}_{3,\boldsymbol{J}} \cdot \boldsymbol{g}_3) \tag{A.18}$$

and finally for the variations of $\boldsymbol{g}_3$:

$$\boldsymbol{g}_{3,\boldsymbol{I}} = \bar{g}_3^{-1}(\tilde{\boldsymbol{g}}_{3,\boldsymbol{I}} - \bar{g}_{3,\boldsymbol{I}}\,\boldsymbol{g}_3) \tag{A.19}$$

$$\boldsymbol{g}_{3,\boldsymbol{I}\boldsymbol{J}} = \bar{g}_3^{-1}(\tilde{\boldsymbol{g}}_{3,\boldsymbol{I}\boldsymbol{J}} - \bar{g}_{3,\boldsymbol{I}\boldsymbol{J}}\,\boldsymbol{g}_3) + \bar{g}_3^{-2}(2\bar{g}_{3,\boldsymbol{I}}\,\bar{g}_{3,\boldsymbol{J}}\,\boldsymbol{g}_3 - \bar{g}_{3,\boldsymbol{I}}\,\tilde{\boldsymbol{g}}_{3,\boldsymbol{J}} - \bar{g}_{3,\boldsymbol{J}}\,\tilde{\boldsymbol{g}}_{3,\boldsymbol{I}}) \tag{A.20}$$

With (A.8)-(A.9) and (A.19)-(A.20), we can compute the variations of the curvatures $b_{\alpha\beta} = \boldsymbol{g}_{\alpha,\beta} \cdot \boldsymbol{g}_3$:

$$b_{\alpha\beta,\boldsymbol{I}} = \boldsymbol{g}_{\alpha,\beta\,,\boldsymbol{I}}\,\boldsymbol{g}_3 + \boldsymbol{g}_{\alpha,\beta}\,\boldsymbol{g}_{3,\boldsymbol{I}} \tag{A.21}$$

$$b_{\alpha\beta,\boldsymbol{I}\boldsymbol{J}} = \boldsymbol{g}_{\alpha,\beta\,,\boldsymbol{I}}\,\boldsymbol{g}_{3,\boldsymbol{J}} + \boldsymbol{g}_{\alpha,\beta\,,\boldsymbol{J}}\,\boldsymbol{g}_{3,\boldsymbol{I}} + \boldsymbol{g}_{\alpha,\beta}\,\boldsymbol{g}_{3,\boldsymbol{I}\boldsymbol{J}} \tag{A.22}$$

With equations (A.8)-(A.9) and (A.21)-(A.22) we finally obtain the variations the strain variables:

$$\varepsilon_{\alpha\beta,\boldsymbol{I}} = \frac{1}{2}(g_{\alpha\beta} - G_{\alpha\beta}),_{\boldsymbol{I}} = \frac{1}{2}g_{\alpha\beta,\boldsymbol{I}} \tag{A.23}$$

$$\varepsilon_{\alpha\beta,\boldsymbol{IJ}} = \frac{1}{2}g_{\alpha\beta,\boldsymbol{IJ}} \tag{A.24}$$

$$\kappa_{\alpha\beta,\boldsymbol{I}} = (B_{\alpha\beta} - b_{\alpha\beta}),_{\boldsymbol{I}} = -b_{\alpha\beta,\boldsymbol{I}} \tag{A.25}$$

$$\kappa_{\alpha\beta,\boldsymbol{IJ}} = -b_{\alpha\beta,\boldsymbol{IJ}} \tag{A.26}$$

Appendix B.

List of used Symbols

B^m	Reference domain of m-dimensional patches, page 4
$B^{(i,p)}$	The i-th B-spline basis of order p, page 3
J	Square root of the determinant of $g_{\alpha\beta}$, page 5
N^i	The i-th NURBS basis function of order p, page 4
V_h^3	Vector isogeometric finite dimensional space with three components, page 5
V_h	Scalar isogeometric finite dimensional space, page 5
$D\mathcal{N}_{\boldsymbol{u}}$	Dirichlet to Neumann map for the fluid system, page 7
Γ^{fsi}	Boundary of the solid domain, page 6
Ω^{f}	Fluid domain, page 6
Ω^{s}	Solid domain, page 6
Ω_0^{s}	Solid reference domain, page 6
Θ	Knot span for B-splines, page 3
α, β	Greek indices, running from zero to one, page 4
$\boldsymbol{\sigma}$	Cauchy stress tensor for the fluid, page 6
$\ddot{\boldsymbol{u}}$	Solid acceleration, page 6
$\boldsymbol{F}$	Solid deformation gradient, page 6
$\delta_\beta^\alpha, \delta_j^i$	Kronecker deltas, page 4
$\dot{\boldsymbol{u}}$	Solid velocity, page 6
η	Fluid viscosity, page 6
$[\![.]\!]$	Jump of a quantity across the middle surface, page 7

$\boldsymbol{g}_\alpha$	Covariant base vectors of the deformed configuration, page 4
$\boldsymbol{i}, \boldsymbol{j}$	Multi-indices (bold latin), where each component i_k, j_k is in the range $[0, n_k)$, page 4
$\boldsymbol{m}$	Bending moments, page 8
$\boldsymbol{n}$	Normal forces, page 8
$\boldsymbol{s}$	Point in the reference domain B^m, page 4
a, b, i, j, k	Latin indices running from one to three, page 4
$b_{\alpha\beta}$	Second fundamental form of the deformed configuration, page 5
$g_{\alpha\beta}$	First fundamental form of the deformed configuration, page 5
h	Shell thickness, page 8
n	Number of univariate B-spline basis, page 3
n_k	Number of B-spline basis functions of the component k for multi-variate B-splines, page 4
p	Degree of B-spline basis (as superscript), page 3
p	Fluid pressure, page 6

References

[1] F. Alouges, A. DeSimone, and L. Heltai. Numerical strategies for stroke optimization of axisymmetric microswimmers. *Mathematical Models and Methods in Applied Science*, 21(02):361–387, 2011.

[2] A. Apostolatos, R. Schmidt, R. Wüchner, and K.-U. Bletzinger. A Nitsche-type formulation and comparison of the most common domain decomposition methods in isogeometric analysis. *International Journal for Numerical Methods in Engineering*, 97:473–504, 2013.

[3] M. Arroyo, A. DeSimone, and L. Heltai. The role of membrane viscosity in the dynamics of fluid membranes. Technical Report 55/2010/M, SISSA, 2010.

[4] M. Arroyo, L. Heltai, D. Millán, and A. DeSimone. Reverse engineering the euglenoid movement. *Proceedings of the National Academy of Sciences*, 109(44):17874–17879, 2012.

[5] F. Auricchio, L. da Veiga, T. Hughes, A. Reali, and G. Sangalli. Isogeometric collocation methods. *Mathematical Models and Methods in Applied Sciences*, 20(11):2075–2107, 2010.

[6] Y. Bazilevs, V. M. Calo, T. J. R. Hughes, and Y. Zhang. Isogeometric fluid-structure interaction: theory, algorithms, and computations. *Computational Mechanics*, 43(1):3–37, 2008.

[7] Y. Bazilevs, M. Hsu, J. Kiendl, R. Wüchner, and K. Bletzinger. 3D simulation of wind turbine rotors at full scale. Part II: Fluid-structure interaction modeling with composite blades. *International Journal for Numerical Methods in Fluids*, 65(1-3):236–253, 2011.

[8] Y. Bazilevs, M.-C. Hsu, J. Kiendl, and D. J. Benson. A computational procedure for prebending of wind turbine blades. *International Journal for Numerical Methods in Engineering*, 89:323–336, 2012.

[9] Y. Bazilevs, M.-C. Hsu, and M. Scott. Isogeometric fluid-structure interaction analysis with emphasis on non-matching discretizations, and with application to wind turbines. *Computer Methods in Applied Mechanics and Engineering*, 249-252:28 – 41, 2012.

[10] Y. Bazilevs, M.-C. Hsu, and M. A. Scott. Isogeometric fluid–structure interaction analysis with emphasis on non-matching discretizations, and with application to wind turbines. *Computer Methods in Applied Mechanics and Engineering*, 249–252:28–41, 2012.

[11] K. Belibassakis, T. Gerostathis, K. Kostas, C. Politis, P. Kaklis, a.I. Ginnis, and C. Feurer. A BEM-isogeometric method for the ship wave-resistance problem. *Ocean Engineering*, 60:53–67, mar 2013.

[12] K. Belibassakis, T. Gerostathis, K. Kostas, C. Politis, P. Kaklis, A. Ginnis, and C. Feurer. A bem-isogeometric method with application to the wavemaking resistance problem of ships at constant speed. In *30th International Conference on Offshore Mechanics and Arctic Engineering, OMAE2011, Rotterdam, The Netherlands*, pages 95 – 102, 2011.

[13] D. Benson, S. Hartmann, Y. Bazilevs, M.-C. Hsu, and T. Hughes. Blended isogeometric shells. *Computer Methods in Applied Mechanics and Engineering*, 255:133–146, 2013.

[14] D. J. Benson, Y. Bazilevs, M. C. Hsu, and T. J. R. Hughes. Isogeometric shell analysis: The Reissner-Mindlin shell. *Computer Methods in Applied Mechanics and Engineering*, 199:276 – 289, 2010.

[15] D. J. Benson, Y. Bazilevs, M.-C. Hsu, and T. J. R. Hughes. A large deformation, rotation-free, isogeometric shell. *Computer Methods in Applied Mechanics and Engineering*, 200:1367 – 1378, 2011.

[16] M. Bischoff, W. Wall, K.-U. Bletzinger, and E. Ramm. Models and finite elements for thin-walled structures. In *Encyclopedia of Computational Mechanics*, volume 2, Solids, Structures and Coupled Problems. Wiley, 2004.

[17] D. Boffi, L. Gastaldi, L. Heltai, and C. S. Peskin. On the hyper-elastic formulation of the immersed boundary method. *Computer Methods in Applied Mechanics and Engineering*, 197(25-28):2210–2231, 2008.

[18] R. Bouclier, T. Elguedj, and A. Combescure. Efficient isogeometric NURBS-based solid-shell elements: Mixed formulation and B-bar-method. *Computer Methods in Applied Mechanics and Engineering*, 267:86–110, Dec. 2013.

[19] M. Breitenberger, A. Apostolatos, B. Philipp, R. Wüchner, and K. Bletzinger. Analysis in computer aided design: Nonlinear isogeometric B-Rep analysis of shell structures. *Computer Methods in Applied Mechanics and Engineering*, 284:401–457, 2015.

[20] J. Caseiro, R. Valente, A. Reali, J. Kiendl, F. Auricchio, and R. Alves de Sousa. On the Assumed Natural Strain method to alleviate locking in solid-shell NURBS-based finite elements. *Computational Mechanics*, 53:1341–1353, 2014.

[21] J. Caseiro, R. Valente, A. Reali, J. Kiendl, F. Auricchio, and R. Alves de Sousa. Assumed Natural Strain NURBS-based solid-shell element for the analysis of large deformation elasto-plastic thin-shell structures. *Computer Methods in Applied Mechanics and Engineering*, 284:861–880, 2015.

[22] H. Casquero, C. Bona-Casas, and H. Gomez. A NURBS-based immersed methodology for fluid-structure interaction. *Computer Methods in Applied Mechanics and Engineering*, 284:943–970, 2015.

[23] L. Chen, N. Nguyen-Thanh, H. Nguyen-Xuan, T. Rabczuk, S. Bordas, and G. Limbert. Explicit finite deformation analysis of isogeometric membranes. *Computer Methods in Applied Mechanics and Engineering*, 277(104-130), 2014.

[24] J. Chung and G. M. Hulbert. A time integration algorithm for structural dynamics with improved numerical dissipation: The generalized-α method method. *Journal of Applied Mechanics*, 60:371–75, 1993.

[25] F. Cirak and M. Ortiz. Fully C1-conforming subdivision elements for finite deformation thin-shell analysis. *International Journal for Numerical Methods in Engineering*, 51:813–833, 2001.

[26] F. Cirak, M. Ortiz, and P. Schröder. Subdivision surfaces: a new paradigm for thin shell analysis. *International Journal for Numerical Methods in Engineering*, 47:2039–2072, 2000.

[27] J. Cottrell, T. Hughes, and Y. Bazilevs. *Isogeometric analysis: toward integration of CAD and FEA*. John Wiley & Sons Inc, 2009.

[28] W. Dettmer and D. Peric. A computational framework for fluid-structure interaction: Finite element formulation and applications. *Computer Methods in Applied Mechanics and Engineering*, 195(41-43):5754 – 5779, 2006.

[29] J. Donea, S. Giuliani, and J. Halleux. An arbitrary lagrangian-eulerian finite element method for transient dynamic fluid-structure interactions. *Computer Methods in Applied Mechanics and Engineering*, 33(1):689 – 723, 1982.

[30] W. Dornisch and S. Klinkel. Treatment of Reissner-Mindlin shells with kinks without the need for drilling rotation stabilization in an isogeometric framework. *Computer Methods in Applied Mechanics and Engineering*, 276:35–66, 2014.

[31] W. Dornisch, S. Klinkel, and B. Simeon. Isogeometric Reissner-Mindlin shell analysis with exactly calculated director vectors. *Computer Methods in Applied Mechanics and Engineering*, 253:491–

504, 2013.

[32] R. Echter, B. Oesterle, and M. Bischoff. A hierarchic family of isogeometric shell finite elements. *Computer Methods in Applied Mechanics and Engineering*, 254(0):170 – 180, 2013.

[33] C. Farhat, M. Lesoinne, and P. L. Tallec. Load and motion transfer algorithms for fluid/structure interaction problems with non-matching discrete interfaces: Momentum and energy conservation, optimal discretization and application to aeroelasticity. *Computer Methods in Applied Mechanics and Engineering*, 157(1-2):95 – 114, 1998.

[34] A. Farutin and C. Misbah. Exact Singularity Subtraction from Boundary Integral Equations in Modeling Vesicles and Red Blood Cells. *Numerical Mathematics: Theory, Methods and Applications*, 7:413–434, 2014.

[35] M. Feischl, G. Gantner, A. Haberl, and D. Praetorius. Adaptive 2D IGA boundary element methods. *arXiv preprint arXiv:1504.06164*, 2015.

[36] M. Feischl, G. Gantner, A. Haberl, and D. Praetorius. Optimal convergence for adaptive IGA boundary element methods for weakly-singular integral equations. *arXiv preprint arXiv: . . .*, 2015.

[37] A. Franci, E. Oñate, and J. M. Carbonell. Unified Lagrangian formulation for solid and fluid mechanics and FSI problems. *Computer Methods in Applied Mechanics and Engineering*, 298:520 – 547, 2016.

[38] T. Greville. Numerical procedures for interpolation by spline functions. *Journal of the Society for Industrial & Applied Mathematics, Series B: Numerical Analysis*, 1(1):53–68, 1964.

[39] Y. Guo and M. Ruess. Nitsche's method for a coupling of isogeometric thin shells and blended shell structures. *Computer Methods in Applied Mechanics and Engineering*, 284:881–905, 2015.

[40] P. Hansbo, J. Hermansson, and T. Svedberg. Nitsche's method combined with space-time finite elements for ALE fluid-structure interaction problems. *Computer Methods in Applied Mechanics and Engineering*, 193(39-41):4195 – 4206, 2004. The Arbitrary Lagrangian-Eulerian Formulation.

[41] L. Heltai. On the stability of the finite element immersed boundary method. *Computers & Structures*, 86(7-8):598–617, apr 2008.

[42] L. Heltai, M. Arroyo, and A. DeSimone. Nonsingular isogeometric boundary element method for Stokes flows in 3D. *Computer Methods in Applied Mechanics and Engineering*, 268:514–539, jan 2014.

[43] L. Heltai and F. Costanzo. Variational implementation of immersed finite element methods. *Computer Methods in Applied Mechanics and Engineering*, 229-232(54/2011/M):110–127, jul 2012.

[44] C. Hesch, A. Gil, A. A. Carreño, and J. Bonet. On continuum immersed strategies for fluid-structure interaction. *Computer Methods in Applied Mechanics and Engineering*, 247-248:51 – 64, 2012.

[45] S. Hosseini, J. Remmers, C. Verhoosel, and R. de Borst. An isogeometric solid-like shell element for nonlinear analysis. *International Journal for Numerical Methods in Engineering*, 95:238–256, 2013.

[46] S. Hosseini, J. Remmers, C. Verhoosel, and R. de Borst. An isogeometric continuum shell element for non-linear analysis. *Computer Methods in Applied Mechanics and Engineering*, 271:1–22, 2014.

[47] M.-C. Hsu and Y. Bazilevs. Fluid–structure interaction modeling of wind turbines: simulating the full machine. *Computational Mechanics*, 50:821–833, 2012.

[48] M.-C. Hsu, D. Kamensky, F. Xu, J. Kiendl, C. Wang, M. Wu, J. Mineroff, A. Reali, Y. Bazilevs, and M. Sacks. Dynamic and fluid-structure interaction simulations of bioprosthetic heart valves using parametric design with t-splines and fung-type material models. *Computational Mechanics*, 55:1211–1225, 2015.

[49] B. Hübner, E. Walhorn, and D. Dinkler. A monolithic approach to fluid-structure interaction using space-time finite elements. *Computer Methods in Applied Mechanics and Engineering*, 193(23-26):2087 – 2104, 2004.

[50] T. Hughes, J. Cottrell, and Y. Bazilevs. Isogeometric analysis: CAD, finite elements, NURBS, exact geometry and mesh refinement. *Computer Methods in Applied Mechanics and Engineering*, 194(39-41):4135–4195, 2005.

[51] T. J. Hughes, W. K. Liu, and T. K. Zimmermann. Lagrangian-Eulerian finite element formulation for incompressible viscous flows. *Computer Methods in Applied Mechanics and Engineering*, 29(3):329 – 349, 1981.

[52] A. Joneidi, C. Verhoosel, and P. Anderson. Isogeometric boundary integral analysis of drops and inextensible membranes in isoviscous flow. *Computers & Fluids*, 2015.

[53] D. Kamensky, M.-C. Hsu, D. Schillinger, J. A. Evans, A. Aggarwal, Y. Bazilevs, M. S. Sacks, and T. J. Hughes. An immersogeometric variational framework for fluid-structure interaction: Application to bioprosthetic heart valves. *Computer Methods in Applied Mechanics and Engineering*, 284:1005–1053, feb 2015.

[54] J. Kiendl, Y. Bazilevs, M.-C. Hsu, R. Wüchner, and K.-U. Bletzinger. The bending strip method for isogeometric analysis of Kirchhoff-Love shell structures comprised of multiple patches. *Computer Methods in Applied Mechanics and Engineering*, 199:2403–2416, 2010.

[55] J. Kiendl, K.-U. Bletzinger, J. Linhard, and R. Wüchner. Isogeometric shell analysis with Kirchhoff-Love elements. *Computer Methods in Applied Mechanics and Engineering*, 198:3902–3914, 2009.

[56] J. Kiendl, M.-C. Hsu, M. Wu, and A. Reali. Isogeometric Kirchhoff-Love shell formulations for general hyperelastic materials. *Computer Methods in Applied Mechanics and Engineering*, 291:280–303, 2015.

[57] G. Kim, C. Lee, and J. Kerwin. A b-spline based higher order panel method for analysis of steady flow around marine propellers. *Ocean Engineering*, 34(14):2045–2060, 2007.

[58] A. Korobenko, M.-C. Hsu, I. Akkerman, J. Tippmann, and Y. Bazilevs. Structural mechanics modeling and FSI simulation of wind turbines. *Mathematical Models and Methods in Applied Sciences*, 23(02):249–272, 2013.

[59] J. Lu and C. Zheng. Dynamic cloth simulation by isogeometric analysis. *Computer Methods in Applied Mechanics and Engineering*, 268:475–493, 2014.

[60] A. Manzoni, F. Salmoiraghi, and L. Heltai. Reduced Basis Isogeometric Methods (RB-IGA) for the real-time simulation of potential flows about parametrized NACA airfoils. *Computer Methods in Applied Mechanics and Engineering*, 284:1147–1180, dec 2015.

[61] B. Marussig, J. Zechner, G. Beer, and T.-P. T. Fries. Fast isogeometric boundary element method based on independent field approximation. *Computer Methods in Applied Mechanics and Engineering*, 284:458–488, 2015.

[62] N. Nguyen-Thanh, J. Kiendl, H. Nguyen-Xuan, R. Wüchner, K. U. Bletzinger, Y. Bazilevs, and T. Rabczuk. Rotation free isogeometric thin shell analysis using PHT-splines. *Computer Methods in Applied Mechanics and Engineering*, 200(47-48):3410–3424, 2011.

[63] N. Nguyen-Thanh, N. Valizadeh, M. Nguyen, H. Nguyen-Xuan, X. Zhuang, P. Areias, G. Zi, Y. Bazilevs, L. De Lorenzis, and T. Rabczuk. An extended isogeometric thin shell analysis based on Kirchhoff–Love theory. *Computer Methods in Applied Mechanics and Engineering*, 284:265–291, 2015.

[64] T. M. Opstal, E. H. Brummelen, R. Borst, and M. R. Lewis. A finite-element/boundary-element method for large-displacement fluid-structure interaction. *Computational Mechanics*, 50(6):779–788, sep 2012.

[65] M. Peake, J. Trevelyan, and G. Coates. Extended isogeometric boundary element method (XIBEM) for three-dimensional medium-wave acoustic scattering problems. *Computer Methods in Applied Mechanics and Engineering*, 2015.

[66] X. Peng, E. Atroshchenko, P. Kerfriden, and S. Bordas. Linear elastic fracture simulation directly from CAD: 2D NURBS-based implementation and role of tip enrichment. Technical report, Cardiff University, 2016.

[67] X. Peng, E. Atroshchenko, and R. Simpson. A two-dimensional isogeometric boundary element method for linear elastic fracture: a path towards damage tolerance analysis without meshing. Technical report, Cardiff University, 2014.

[68] L. Piegl and W. Tiller. *The NURBS book (2nd ed.)*. Springer-Verlag New York, Inc., New York, NY, USA, 1997.

[69] C. Politis, A. I. Ginnis, P. D. Kaklis, K. Belibassakis, and C. Feurer. An isogeometric bem for exterior potential-flow problems in the plane. In *2009 SIAM/ACM Joint Conference on Geometric and Physical Modeling*, SPM '09, pages 349–354, New York, NY, USA, 2009. ACM.

[70] C. Pozrikidis. *Boundary integral and singularity methods for linearized viscous flow*. Cambridge Texts in Applied Mathematics. Cambridge University Press, Cambridge, 1992.

[71] N. Rotundo, T.-Y. Kim, W. Jiang, L. Heltai, and E. Fried. Error estimates of b-spline based finite-element method for the wind-driven ocean circulation. Technical report, Weierstrass Institute for Applied Analysis and Stochastics, 2015.

[72] R. Schmidt, J. Kiendl, K.-U. Bletzinger, and R. Wüchner. Realization of an integrated structural design process: analysis–suitable geometric modelling and isogeometric analysis. *Computing and Visualization in Science*, 13(7):315–330, 2010.

[73] O. Steinbach. *Numerical approximation methods for elliptic boundary value problems: finite and boundary elements*. Springer Verlag, 2008.

[74] T. Takahashi and T. Matsumoto. An application of fast multipole method to isogeometric boundary element method for laplace equation in two dimensions. *Engineering Analysis with Boundary Elements*, 36(12):1766 – 1775, 2012.

[75] K. Takizawa and T. E. Tezduyar. Multiscale space–time fluid–structure interaction techniques.

Computational Mechanics, 48(3):247–267, 2011.

[76] K. Takizawa and T. E. Tezduyar. Computational Methods for Parachute Fluid–Structure Interactions. *Archives of Computational Methods in Engineering*, 19(1):125–169, 2012.

[77] T. E. Tezduyar. Finite element methods for flow problems with moving boundaries and interfaces. *Archives of Computational Methods in Engineering*, 8(2):83–130, 2001.

[78] T. E. Tezduyar, M. Behr, and J. Liou. A new strategy for finite element computations involving moving boundaries and interfaces - The deforming-spatial-domain/space-time procedure: I. The concept and the preliminary numerical tests. *Computer Methods in Applied Mechanics and Engineering*, 94(3):339 – 351, 1992.

[79] T. E. Tezduyar, M. Behr, S. Mittal, and J. Liou. A new strategy for finite element computations involving moving boundaries and interfaces - The deforming-spatial-domain/space-time procedure: II. Computation of free-surface flows, two-liquid flows, and flows with drifting cylinders. *Computer Methods in Applied Mechanics and Engineering*, 94(3):353 – 371, 1992.

[80] T. E. Tezduyar, S. Sathe, R. Keedy, and K. Stein. Space - time finite element techniques for computation of fluid - structure interactions. *Computer Methods in Applied Mechanics and Engineering*, 195(17 - 18):2002 – 2027, 2006.

[81] T.-K. Uhm and S.-K. Youn. T-spline finite element method for the analysis of shell structures. *International Journal for Numerical Methods in Engineering*, 80:507–536, 2009.

[82] T. van Opstal and E. van Brummelen. A finite-element/boundary-element method for large-displacement fluidstructure interaction with potential flow. *Computer Methods in Applied Mechanics and Engineering*, 266:57–69, nov 2013.

[83] T. van Opstal, E. van Brummelen, and G. van Zwieten. A finite-element/boundary-element method for three-dimensional, large-displacement fluidstructure-interaction. *Computer Methods in Applied Mechanics and Engineering*, 284:637–663, 2015.

[84] Y. Wang and D. Benson. Multi-patch nonsingular isogeometric boundary element analysis in 3D. *Computer Methods in Applied Mechanics and Engineering*, 2015.

[85] Y. Wang, D. Benson, and A. Nagy. A multi-patch nonsingular isogeometric boundary element method using trimmed elements. *Computational Mechanics*, 2015.

[86] L. Zhang, A. Gerstenberger, X. Wang, and W. K. Liu. Immersed finite element method. *Computer Methods in Applied Mechanics and Engineering*, 193(21-22):2051 – 2067, 2004.